Materials and Design 199 (2021) 109415

Contents lists available at ScienceDirect

Materials and Design

journal homepage: www.elsevier.com/locate/matdes

# Investigation on *in-situ* sprayed, annealed and corona poled PVDF-TrFE coatings for guided wave-based structural health monitoring: From crystallization to piezoelectricity

Yehai Li [a,b,c], Wei Feng [b,c,*], Long Meng [d], Kwong Ming Tse [e], Zhen Li [a,b,c], Linbing Huang [a,b,c], Zhongqing Su [f], Shifeng Guo [a,b,c,*]

[a] Shenzhen Key Laboratory of Smart Sensing and Intelligent Systems, Shenzhen Institutes of Advanced Technology, Chinese Academy of Sciences, Shenzhen 518055, PR China
[b] CAS Key Laboratory of Human-Machine Intelligence-Synergy Systems, Shenzhen Institutes of Advanced Technology, Shenzhen 518055, PR China
[c] Guangdong Provincial Key Lab of Robotics and Intelligent System, Shenzhen Institutes of Advanced Technology, Chinese Academy of Sciences, Shenzhen 518055, PR China
[d] Paul C. Lauterbur Research Center for Biomedical Imaging, Shenzhen Institutes of Advanced Technology, Chinese Academy of Sciences, Shenzhen 518055, PR China
[e] Department of Mechanical and Product Design Engineering, Swinburne University of Technology, Hawthorn, Melbourne, Victoria 3122, Australia
[f] Department of Mechanical Engineering, The Hong Kong Polytechnic University, Hung Hom, Kowloon 999077, Hong Kong Special Administrative Region

## HIGHLIGHTS

- *In-situ* fabrication and functionalization of piezopolymer coatings.
- Optimized crystallization and piezoelectricity by annealing and corona poling.
- Light, thin, flexible, consistent, rapid-prototyping and adhesive-free sensing networks.
- High adaptive, high consistent performance of actuation and sensing guided waves with negligible inter-path interference.

## GRAPHICAL ABSTRACT

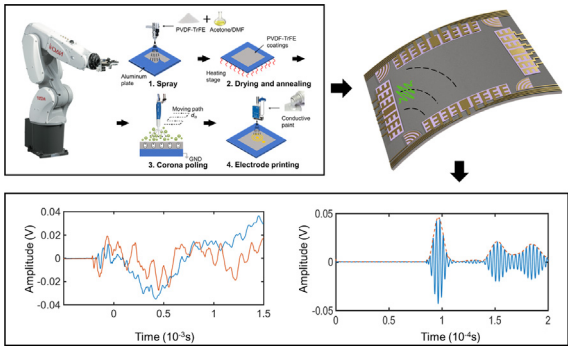


## ARTICLE INFO

*Article history:*
Received 12 August 2020
Received in revised form 14 December 2020
Accepted 15 December 2020
Available online 16 December 2020

*Keywords:*
PVDF-TrFE coatings
*In-situ* fabrication and functionalization
Crystallization
Piezoelectricity
Sensing networks
Guided waves-based structural health monitoring

## ABSTRACT

Large-area, lightweight and flexible sensing networks are highly demanded in complex (either in structural topology or material property) structural health monitoring (SHM) applications. Development of piezopolymer offers a feasible solution. In pursuit of maximum exploitation of their functionality, the optimal fabrication technique requires to be investigated first. In this study, PVDF-TrFE coatings were *in-situ* fabricated and directly functionalized on structural surfaces in the consecutive processing steps as spray, thermal annealing, and corona poling. The processing conditions, including annealing temperature/time and poling voltage/duration, were correlated with their crystallinity, ferroelectric phase, morphology, polarization, and final piezoelectricity, through a systematic study. With the help of various characterization methods, the conditions of optimal functional performance were identified and rationalized. To study the feasibility of thus-prepared functional coatings in transducing guided waves, the host structures with sensors made of such coatings were interrogated by passive acoustic emission and active ultrasonic transmission to validate the sensing and actuation capability, respectively. The developed piezopolymer coatings possess excellent performance as a novel configuration of sensing networks, with lightweight, ultrathin, flexible, rapid-prototyping and adhesive-free features, manifesting high adaptability, high consistency, negligible inter-path interference, and minimal extra penalty for a robust SHM system.

* Corresponding authors at: Shenzhen Key Laboratory of Smart Sensing and Intelligent Systems, Shenzhen Institutes of Advanced Technology, Chinese Academy of Sciences, Shenzhen 518055, PR China.
*E-mail addresses:* wei.feng@siat.ac.cn (W. Feng), sf.guo@siat.ac.cn (S. Guo).

https://doi.org/10.1016/j.matdes.2020.109415

## 1. Introduction

Due to the strong electro-mechanical coupling ability, piezomaterials have been widely used to generate and/or receive guided waves for structural health monitoring (SHM) applications in engineering structures [1–3]. Their competence in sensing and actuation is crucial to achieve an effective SHM system. Conventional piezoceramics with high density and brittleness have their practical shortcomings associated with mass/volume loadings, incompatibility with large strain, and poor conformity with non-flat or complex surfaces, especially for the aerospace structures with high design criteria. Recently, there has been a growing emphasis on piezopolymers, due to their high flexibility, ultra-light weight, ultra-low profile, low cost, high manufacturability *etc.* Polyvinylidene fluoride (PVDF) and its copolymer with trifluoroethylene (TrFE), PVDF-TrFE, are the most widely investigated piezopolymers due to their good polarization and solvent compatibility. Unlike the polymorphic PVDF, PVDF-TrFE consists mostly of ferroelectric phase at room temperature, which makes it easier to obtain piezoelectricity and being spared from phase transformation processes such as mechanical stretching [4] or addition of nanofillers [5]. Thus, PVDF-TrFE has gained substantial favour with researchers in developing functional materials. Yet its ferroelectric crystallization and piezoelectric performance are strongly perturbed by the manufacture methods and processing conditions. Such an intriguing topic has been studied extensively by many researchers, giving rise to different speculations and controversies.

As a semi-crystalline polymer, thermal annealing treatment is an important process for PVDF-TrFE to enhance crystallinity and ferroelectric phase. The annealing temperature controls the phase transition of crystal structures. Below Curie temperature ($T_c$), ferroelectric phase (orthorhombic crystal structure) is dominant and the chain conformation is *all-trans* (TTTTT), similar to the β phase of PVDF. Above $T_c$, ferroelectric phase changes to paraelectric phase (hexagonal crystal structure) containing a number of *gauche* linkages ($TG^+$ or $TG^-$) [6]. Most researchers have reached a consensus that the annealing temperature of PVDF-TrFE should be above $T_c$, at which molecular chains in amorphous phase are mobile enough to rearrange themselves into electroactive crystalline phase, and below the melting temperature ($T_m$), exceeding which the reorientation of lamellar chains causes irreversible extinction of ferroelectric polarization [7]. However, the most suitable annealing temperature of PVDF-TrFE to achieve high piezoelectricity varies from case to case. Mao et al. [8] concluded that annealing above $T_c$ caused increasing in crystallinity with increasing temperature (below $T_m$). However, the highest remnant polarization reached saturation just at $T_c$ (118 °C). Interestingly, Mahdi et al. [9] observed that both crystallinity and remnant polarization reached the highest value with annealing temperature slightly above $T_c$ at 100 °C ($T_c$ = 90 °C, $T_m$ > 140 °C) and decreased with higher annealing temperature. Similar trends were also obtained by *Ng* et al. [10] which reported that the optimal annealing temperature was at $T_c$ (120 °C). On the other hand, others found that the piezoelectricity-related property (piezoelectric constant or remnant polarization) continued to increase with annealing temperature increasing above $T_c$ but below $T_m$, and the optimal annealing temperature was in the middle of $T_c$ and $T_m$ as, just to mention a few, 130 °C ($T_c$ = 94 °C, $T_m$ = 151 °C) [11], 135 °C ($T_c$ = 115 °C, $T_m$ = 150 °C) [12], 140 °C [13]. Annealing time is another debated issue and mostly depends on empirical observations. It can range from 30 min [14], to 1 h [9], to 2 h [8,11,13,15], and up to 5 h [16]. Some researchers annealed overnight as long as 12 h [17] or 24 h [18] to attempt full transfer of amorphous phase. On the contrary, Spampinato et al. [12] asserted that only 15 min was enough to induce a high degree of crystallinity and remnant polarization. Longer annealing treatment would not lead to functional improvement but rather deterioration, as increasing coercive field.

Proper annealing treatment could enhance the ferroelectric phase in PVDF-TrFE, which still exhibits little macroscopic piezoelectricity, with the dipoles in polar crystalline regions of ferroelectric phase in random orientation (originated from the large difference in electronegativity between fluorine and hydrogen with respect to carbon). The overall piezoelectricity of piezopolymer arises from remnant polarization, *i.e.*, net dipole moment after high-voltage poling treatment. Typical poling methods include direct-contact thermal poling and non-contact corona poling. In thermal poling, the sample with attached electrodes on both sides is directly connected to a high DC voltage. Usually, the whole sample is submerged in a silicon oil bath with elevated temperature to avoid breakdown of surrounding air. Corona poling is performed by locating a high-voltage metal needle above the sample, with only the bottom electrode required and grounded. The ionization of air around the needle tip generates charge ions which are collected on the polymer surface and form poling electrical field. With poling treatment, crystalline structural features of piezopolymers such as chain conformation, microstructural packing density, crystallinity, molecular chain orientation, and crystal size would be influenced by the rotation of dipoles under the electric field [19], some of which directly impact the overall electrical properties of piezopolymers. Thus, appropriate poling conditions are also considered as a potential method for enhancing ferroelectric crystalline structure and final piezoelectricity. Kim et al. [20] concluded that stronger electric voltage resulted in higher piezoelectric coefficient while the elevated bed temperature in corona poling process reduced the piezoelectricity. Mahadeva et al. [21] found that the piezoelectric constant increased with poling time and reached a saturation value at 45 min. Moreover, Ducrot et al.'s work [22] had shown that with a sufficiently strong electric field, the necessary poling duration was very short (about 5 min).

Most manufacture techniques of piezopolymer are developed as solution-based methods, because piezopolymer is highly soluble to common organic solvents. Spin coating has been treated as an effective method, due to the shear effect induced which could accelerate crystallization [8,23,24]. Electrospinning has its advantages as strong mechanical stretching force and electrical poling field during the manufacturing process naturally align dipoles and enhance the ferroelectric phase, eliminating need for post-treatment process [11,25,26]. However, these free-standing films were surface-mounted on or embedded in the structure materials using adhesives or couplant for sensing [27,28], which will greatly affect the consistency and reproducibility.

Another fabrication family, namely 3D printing technology, originated from additive manufacturing, has drawn attention recently due to unique adhesive-free and rapid-prototyping features, including inkjet [29], spray [30,31], and fused deposition modeling [20]. The automated processes guarantee the consistency of installed sensing elements, which could greatly improve the measuring error due to non-uniform thickness and quality of couplant or bonding layer in manually installed sensors [32,33].

Despite those previous studies, there is no systematic study on the processing conditions of sprayed piezopolymer coatings with thermal annealing and corona poling treatments, which optimizes the crystalline and piezoelectric properties. It is of interest to ascertain whether consistent results as in previous studies fabricated by other methods can be expected, and to investigate the feasibility of thus-prepared coatings for sensing and actuation in SHM applications. Such studies are an indispensable tool for exploiting the utmost of the functionality of piezopolymer coatings. In this study, PVDF-TrFE coatings are *in-situ*

fabricated as an intelligent sensing layer directly on inspected structures along with spray, annealing, and corona poling as the functionalization processes. The multiple cases of processing conditions including annealing temperature/time and poling voltage/duration are discussed, referring to correlation with the crystallization and final piezoelectric properties of PVDF-TrFE coatings, by a dedicated design of experiments and comprehensive characterization methods. Then, the processing conditions that result in optimal piezoelectric performance are identified and applied to prepare PVDF-TrFE coatings on structures to form sensors and actuators. Passive acoustic emission is used to test the capability of capturing guided waves, whilst active ultrasonic transmission is used to test the capability of exciting ultrasonic guided waves. Lead zirconate titanate (PZT) wafers, the conventional piezoelectric sensors for SHM networks, were compared with PVDF-TrFE coatings in three aspects: adaptability to specific waves, consistency, and interference to wave propagation. The feasibility and advantages of *in-situ* fabrication and functionalization of piezopolymer in the form of coatings for SHM are discussed, in a novel configuration of large-area, high-density, high adaptive and high consistent sensing networks.

## 2. Experimental section

### 2.1. In-situ fabrication and functionalization

Raw PVDF-TrFE (70/30 mol%) was obtained from Piezotech® in the form of white pellets. These pellets were dissolved in *N*,*N*-Dimethylformamide (DMF, Sigma-Aldrich) and acetone (50/50 vol%) by magnetic stirring at room temperature for 6 h to achieve a clear solution at a concentration of 5 wt%. DMF was a highly effective solvent for PVDF-TrFE, while acetone was used to dilute the mixture of PVDF-TrFE and DMF, in order to adjust the viscosity for spray purpose. The solution with proper volume was sprayed on cleaned and polished aluminium plates to form thin piezopolymer coatings. Then the specimen was placed on a heating stage at 80 °C to vaporize any remaining solvent. By controlling the spray quantity and speed, the thickness of thus-sprayed PVDF-TrFE coatings was about 20 μm as measured by a profilometer (Bruker DektakXT). After drying, the pristine coatings (without annealing or poling treated) were used as a reference sample (denoted as Ref. hereafter) for crystallization analysis. The PVDF-TrFE coatings were then annealed at different temperatures for different time and cooled down slowly to room temperature. Since the metal structure itself could be treated as the bottom electrode, polarization was conducted directly by corona poling treatment, which was easier to operate and more suitable for *in-situ* functionalization than thermal poling treatment to achieve the piezoelectricity. Finally, the up-surface electrode was printed on using a commercial Cu—Ag conductive paint. The whole *in-situ* fabrication and functionalization process of PVDF-TrFE coatings is illustrated below in Fig. 1.

Corona poling was performed by a metal needle placed 3 cm above the grounded specimen. The needle was connected to a high DC voltage to enable ionization of surrounding air. Since the large-area functional coatings were favoured when building sensing networks on structures, in this study, rather than using a metal grid for uniform distribution of ions, the highly charged needle was controlled by a robot arm and travelled in a meandering path to cover the to-be-functionalized area, as shown in Fig. 1. However, in order to determine the proper length of the lateral span $d_{ls}$, the effective poling range by a static needle was investigated first. The sprayed and annealed coatings were in the rectangular shape of 5 cm × 5 cm, with the high-voltage needle holding in the central location for 10 min. Then a circular up-surface electrode was painted with a diameter of 3 cm. The vertical displacement under driven voltage was measured along the diameter direction by a laser scanning vibrometer (detailed in the next section) to calibrate the polarization, as illustrated in Fig. 2.

It is clear to observe that the piezoelectricity remains stable within 5 mm around the central poling location and decreases quickly outside this range. Thus, the moving pattern of high-voltage metal needle was set at 10 mm/s with $d_{ls}$ of 10 mm. The meandering path was travelled repeatedly to enhance the polarization. To investigate the poling effect, the poling voltage applied on the needle and repeated cycle number were varied.

### 2.2. Characterization

The thermal behaviour of thus-sprayed PVDF-TrFE coatings was characterized with a differential scanning calorimeter (DSC, TA

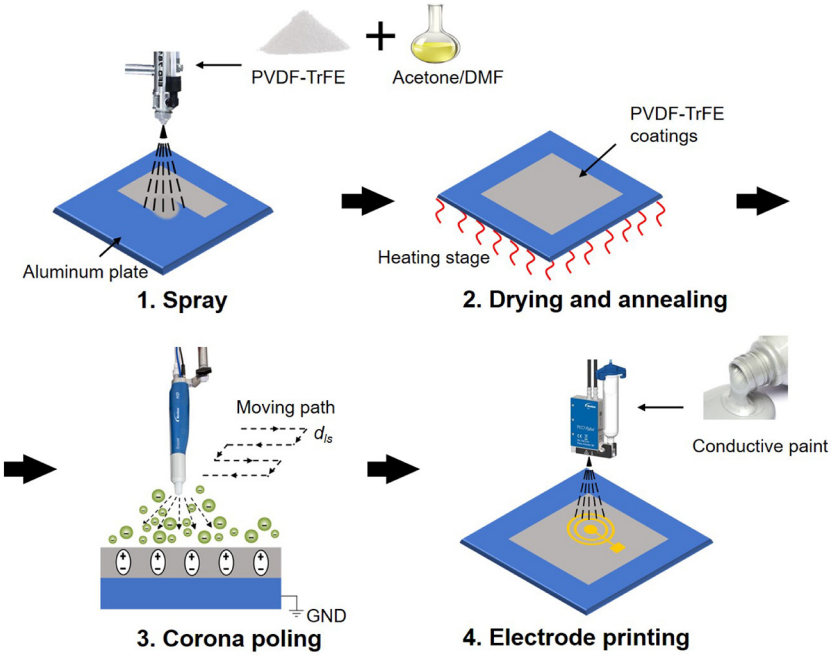


**Fig. 1.** *In-situ* fabrication and functionalization of PVDF-TrFE coatings.

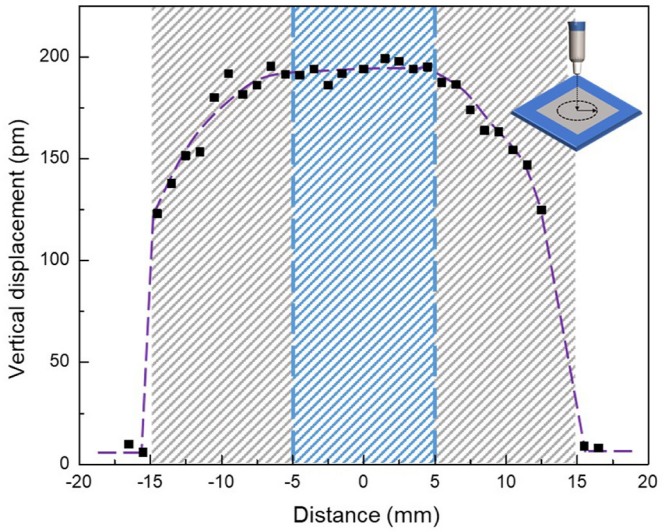


**Fig. 2.** *In-situ* corona poling effect of PVDF-TrFE coatings as measured vertical displacement with distance from the poling spot. The grey shaded area is the up-surface electrode covering range. The blue shaded area indicates the stable piezoelectricity range.

Instruments Q20), at temperature ranging from 30 °C to 170 °C, at a rate of 10 °C/min under a 50 mL/min nitrogen gas flow. DSC data was analyzed using Universal Analysis Software (TA Instruments). From DSC curves, $T_c$ and $T_m$ can be measured through identifying the endothermic peaks with increasing temperature, which appear during ferroelectric-paraelectric transitioning and melting. Crystallization of thus-sprayed, annealed and corona poled PVDF-TrFE coatings was examined by an X-ray diffractometer (XRD, Bruker D8 Advance). The X-ray angle (2Theta) was varied between 15° and 70° with a resolution of 0.02°. The degree of crystallinity ($\chi_c$) for each sample was calculated based on the relative areas under the amorphous and crystalline peaks of XRD spectra [9,12]. Field Emission Scanning Electron Microscope (FESEM, ZEISS SUPRA® 55) was used to study the morphology of piezopolymer coatings under different annealing treatments. With 50 K magnification, the crystalline structure can be observed clearly.

Since the PVDF-TrFE coatings were aimed for dynamic wave-based applications, piezoelectricity was analogously determined through a dynamic measurement method [34], *i.e.,* measuring piezoelectric constant $d_{33}$ *via* a laser scanning vibrometer (Polytec UHF-120) (Fig. 3), to avoid the error from static measurement due to possible resonance. The thus-prepared aluminium plate with PVDF-TrFE coatings was placed on an XY platform, with the up-surface electrode connected to a driven signal and the uncoated part of the metal specimen grounded. The laser vibrometer measured the vertical displacement of surface within a small area across the boundary of the electrode, as shown in Fig. 3a. Fig. 3b shows the typical results with a sinusoidal driven signal of 100 kHz and 10 V. The inverse piezoelectric effect can be expressed by

$$S = s^E T + dE, \tag{1}$$

where $S$ and $T$ are the strain and stress; $s^E$ is the compliance under constant electric field; $d$ is the electro-mechanical coupling coefficient, also known as piezoelectric constant; $E$ is the electrical field. For vertical poled piezomaterials, $d_{33}$ can be calculated by measuring the vibration response under a sinusoidal driven signal as

$$d_{33} = \frac{E_3}{S_3} = \frac{U_z/t}{u_z/t} = \frac{U_z}{u_z}, \tag{2}$$

where $E_3$ and $S_3$ represent the electric field and strain respectively in thickness or vertical direction; $t$ is the thickness of measured coatings; $U_z$ and $u_z$ are the driven voltage and displacement in the vertical direction. PVDF and its copolymer PVDF-TrFE with small thickness and low modulus are proven to possess extremely high resonance frequency and flat frequency response over a wide range of frequency [35–37]. In order to validate such frequency independence of thus-prepared PVDF-TrFE coatings in this study and to select a suitable driven signal in the proposed piezoelectricity characterization method, the driving frequency was swept from 50 kHz to 1 MHz, which was also the common frequency range of diagnostic ultrasonic guide waves in SHM. It is shown in Fig. 3c that the measured piezoelectric constant $d_{33}$ has a stable value of about 19.4 ± 1.5 pm/V within such a frequency band. Thus, 100 kHz was selected as the frequency of the driven signal with a voltage of 10 V for the piezoelectricity characterization in the following experiments.

### 2.3. Guided waves sensing and actuation

Without loss of generality, typical guided wave experiments were conducted to validate the sensing and actuation performance of thus-prepared coatings, and also to demonstrate how to implement their versatility in guided wave-based SHM. The functional coatings were *in-situ* fabricated on a beam specimen (200 mm × 50 mm × 2 mm) with monolithic up-surface electrodes for broadband applications such as passive acoustic emission (AE). Pencil lead breaks were used to simulate AE source *via* pressing a 0.5-mm diameter pencil lead approximately 3 mm from its tip against the specimen. This test is generally used to validate the accuracy and sensitivity of sensors. As shown in Fig. 4a, guided waves were generated *via* lead breaking and captured by two sensors made of PVDF-TrFE coatings *via* an oscilloscope (Tektronix MDO3000). For out-of-plane sources such as impact, AE signals were simulated with a lead break on the surface. For simulating in-plane sources such as cracking, the lead was fractured on the mid-plane of the edge. The actuation performance of thus-prepared coatings was validated in an active ultrasonic transmission test (Fig. 4b). Comb-like electrodes were prepared on coatings matching with wavelength pre-selected for narrowband applications. Guided ultrasonic waves (GUWs) were carried out by injecting elastic waves into the beam structure at one end, by RITEC RAM-5000 Computer Controlled Ultrasonic System, including a signal generator module and an amplifier module, and monitoring response signals at the other end, after waves propagating by an oscilloscope (Tektronix MDO3000), in a typical pitch-catch mode. A mass block was used as an artificial defect and placed on the transmission path. Such additional mass is a typical kind of artificial defect in verification experiments [38]. It can be reinstalled in different locations without damaging the structures and used repeatedly.

## 3. Results and discussion

### 3.1. Thermal annealing treatment

A hot plate was used for temperature control of samples in thermal annealing treatment in this study. For different *in-situ* circumstances, an environmental chamber or an infrared heating lamp would be feasible alternatives. The annealing variables, temperature and time, were investigated individually by fixing the other. After that, both variables were controlled and crossed at the same time based on the design of experiments. Their effect on the crystallization and piezoelectricity of thus-prepared PVDF-TrFE coatings was investigated and summarized, to determine the suitable processing conditions which could benefit the final functionality for SHM applications.

#### 3.1.1. Annealing temperature

Fig. 5 shows the DSC results of as-received PVDF-TrFE powder and thus-sprayed Ref. coatings. Although similar $T_m$ peak at about 150 °C can be observed, the $T_c$ peak of coatings shifts higher than of as-received powder. This could be attributed to the more perfect and stable

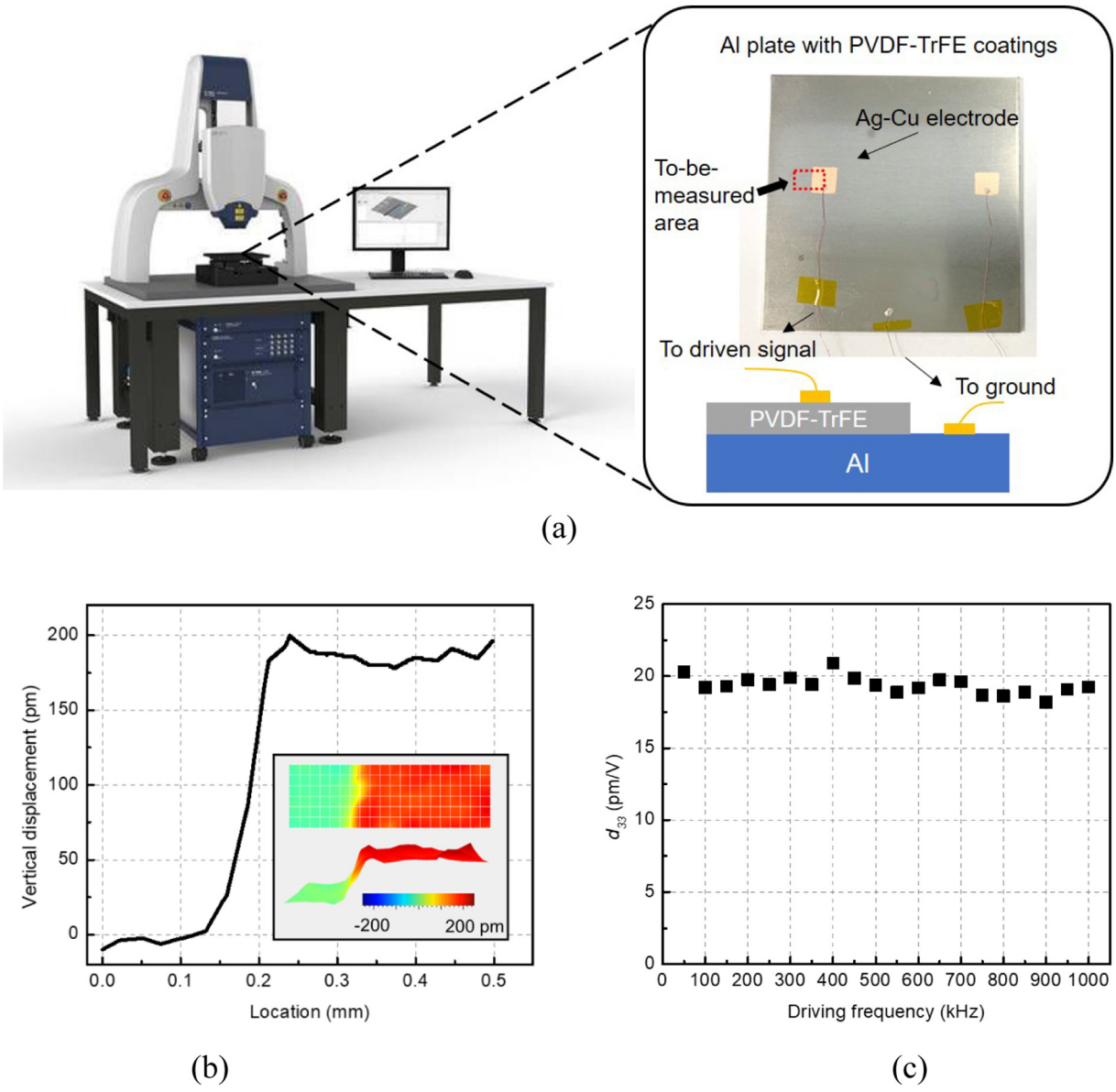


**Fig. 3.** Piezoelectric constant measurement: (a) prepared aluminium plate with PVDF-TrFE coatings placed on the platform of a laser vibrometer. Red rectangle area is the interested place for measurement; (b) typical results of measured vertical displacement across the boundary of the up-surface electrodes which are connected to a sinusoidal driven signal of 100 kHz and 10 V. Inset: three-dimensional contour view; (c) sweep test results of calculated $d_{33}$ *versus* driving frequencies.

crystallites formed after the spray and drying process. The new $T_c^{'}$ peak appears broad, ranging from 107 °C to 110 °C, due to defects in ferroelectric phase [39]. Thus, to investigate annealing treatment, the annealing temperature was varied as 110 °C, 120 °C, 130 °C, 140 °C, and 170 °C. Since the Ref. sample was sprayed and dried at 80 °C, it could be regarded as annealed below $T_c$ at 80 °C. The annealing time was set as 2 h for all samples.

In XRD spectra with 2Theta from 15° to 70° only one obvious peak is identified for all annealed samples. As shown in Fig. 6a, the intensities of samples annealed at and above 120 °C are apparently stronger, and the peak location shifts from about 20.0° to 19.9°. This peak is assigned to the (110) and (200) plane reflections of the crystals in the ferroelectric phase. Peak shifting to a lower value is related to the slight increase in interchain spacing, caused by *gauche* defects induced in the ferroelectric phase during paraelectric-ferroelectric transition after cooling down from annealing [40]. The shoulder of the peak presented is related to the amorphous region. Therefore, to qualify the degree of crystallinity, this peak is fitted and deconvoluted into the sum of crystalline phase peak and amorphous phase peak by pseudo-Voigt function (Fig. 6b). The degree of crystallinity $\chi_c$ can be calculated as

$$\chi_c = \frac{A_c}{A_c + A_m}, \tag{3}$$

where $A_c$ and $A_m$ are the integrated areas of the respective fitted peak of crystalline phase and amorphous phase. Since only ferroelectric phase exists in PVDF-TrFE below $T_c$, calculated ferroelectric crystallinity corresponds to the total crystallinity. The results are displayed in Fig. 6c, where the degree of crystallinity increases abruptly and also reaches saturation for annealing at 120 °C. Interesting, neither the peak intensity nor the degree of crystallinity shows decrease for annealing at 170 °C (above $T_m$). This observation is consistent and aligns well with the

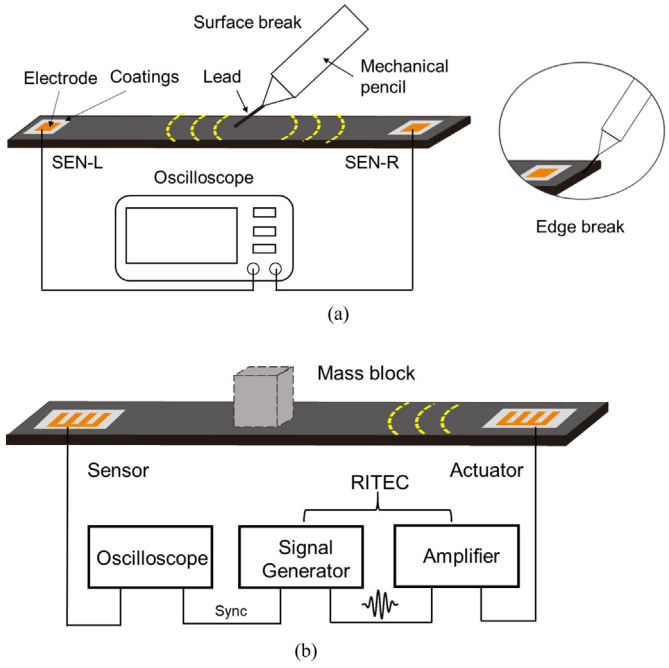


**Fig. 4.** Illustration of (a) passive acoustic emission test and (b) active ultrasonic transmission test.

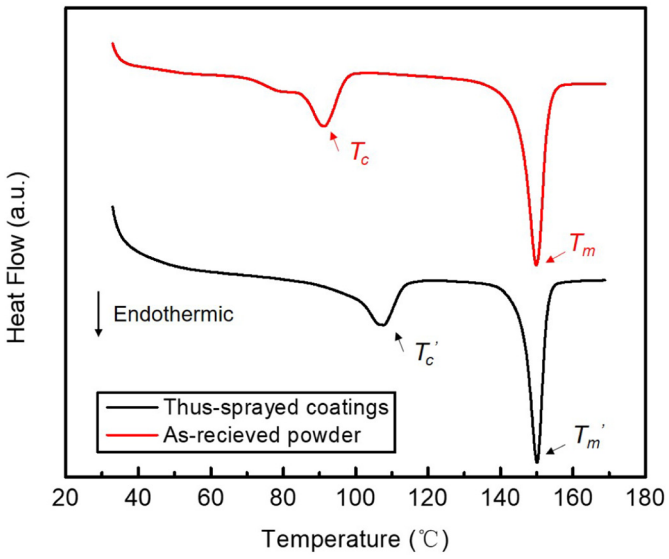


**Fig. 5.** DSC curves of as-received PVDF-TrFE powder and thus-sprayed Ref. coating sample.

results in some reported studies [11,41,42], while disagreeing with those in some others [8,9].

To correlate with final piezoelectricity, the annealed samples were corona poled at 35 kV for 5 cycles. Considering the possible difference arisen from non-uniformly treated coatings, at least three different locations of the samples were measured by the proposed piezoelectricity characterization method and the corresponding results were statistically integrated. The results of measured piezoelectric constant $d_{33}$ are shown in Fig. 6d. It is anticipated that the increase in the degree of crystallinity due to annealing will consequently increase polarization which is linearly proportional to the piezoelectricity, given that more dipoles available. The annealing temperature at 110 °C (around $T_c$) did cause marginal increase in the crystallinity and piezoelectricity, however, large deviation in piezoelectricity can be observed, which can be explained by the fluctuation of temperature control during annealing process, providing unstable and inconsistent transitioning energy at $T_c$. With increasing annealing temperature, the piezoelectricity of samples has a similar pattern with crystallinity, except for samples annealed at 170 °C, of which the crystallinity remains at a high level while the piezoelectricity deceases extensively. Moreover, these results also indicate that the poling condition used here is sufficient to rotate dipoles in ferroelectric phase.

FESEM micrographs could provide more insights about crystallization by annealing treatment. As shown in Fig. 7, micrographs of samples annealed at 110 °C, 120 °C, 130 °C, 140 °C, and 170 °C were compared with unannealed Ref. sample. Without annealing treatment, the coatings are constituted of small granules. Combined with the XRD results, it can be deduced that the coatings are not well crystallized. When the annealing temperature approaches 110 °C (around $T_c$), part of crystallites grow into sparse and small fibrillar grains with a size of approximately 100 nm in length and 20 nm in width, but still large non-crystallized domains are observed, which can be attributed to the amorphous phase in XRD results. With further increase in the annealing temperature, the granular crystallites develop into dense and ellipsoidal grains, and grow larger in size (~150 nm in length and 40 nm in width for 120 °C and ~200 nm in length and 50 nm in width for 140 °C). Such crystalline structure is known to be the characteristic morphology of edge-on lamella which are formed by stacks of folded chains of PVDF-TrFE molecules parallel to the substrate surface [43]. The formation of enlarged and increased crystalline structures enhances the crystallinity properties of PVDF-TrFE coatings, which is consistent with the aforementioned XRD results. This suggests that annealing between $T_c$ and $T_m$ induces growth in small crystallites as a result of the coalescence of neighboring crystallites and incorporation of surrounding non-crystalline molecules, while undergoing a transition into the paraelectric phase. Although higher annealing temperature favors larger crystallites, it could not contribute to any further increase in the crystallinity degree, as indicated by the plateau in Fig. 6c. Besides it could increase surface roughness, which would result in the increased leakage current [8]. Annealing at temperature above $T_m$ at 170 °C results in PVDF-TrFE coatings with a completely different morphology. Significantly long rod-like crystallites are formed (~ 5 μm in length and 150 nm in width) and further intercrossed in a bird's nest configuration, while undergoing the melting and recrystallization process when annealed above $T_m$. According to previous studies [8,41,44], the long rod crystalline structures here are consisting of extended chains, and still belong to the edge-on lamella. However, the other smooth domains are attributed to the face-on lamellar crystalline structures, where the chain axis is reoriented normal to the substrate surface, which would not contribute to polarization in the thickness direction [45]. This also explains the high-level crystallinity and low-level piezoelectricity for samples annealed at 170 °C, as exhibited in Fig. 6. The results show that annealing temperature at 120 °C, 130 °C, and 140 °C could provide strong crystallinity and piezoelectricity.

### 3.1.2. Annealing time

According to the annealing temperature results discussed in the preceding section, the various annealing time, such as 15 min, 30 min, 1 h, 2 h, and 4 h at temperature of 120 °C, spanning across the most commonly reported annealing duration in the literature, were investigated. As seen in Fig. 8a and b, both the crystallinity and piezoelectricity reach their saturation after 1 h annealing. Further annealing would not increase either crystallinity or piezoelectricity. Similar trends can be observed from FESEM micrographs in Fig. 9. After 15 min annealing, PVDF-TrFE coatings still possess large and many non-crystalline domains. With longer annealing time, the crystallites array tighter and plumper, and non-crystalline domains become less and smaller. For 1 h and longer annealing time, only small and few non-crystalline domains remain, and no obvious difference in crystallites can be observed, which implies the saturation of crystallization. Hence, for annealing

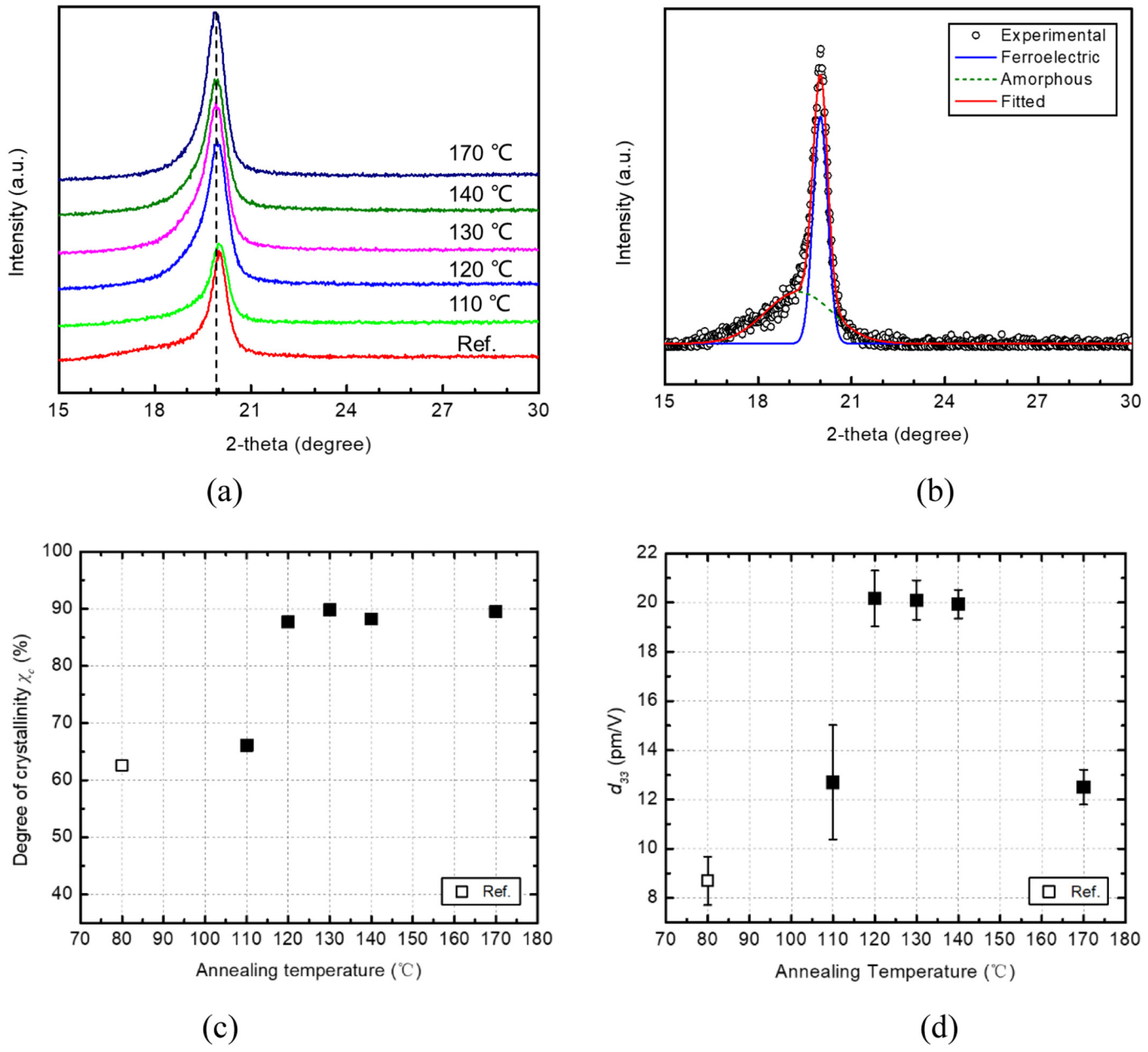


**Fig. 6.** (a) XRD results of PVDF-TrFE coatings subjected to various annealing temperatures; (b) peak fitting and deconvolution of XRD curve of Ref. sample; (c) calculated degree of crystallinity of PVDF-TrFE coatings subjected to various annealing temperatures; (d) measured piezoelectric constant $d_{33}$ of PVDF-TrFE coatings subjected to various annealing temperatures after poling treatment.

temperature of 120 °C, 1 h annealing time is sufficient to achieve optimal functionality of PVDF-TrFE coatings.

### 3.1.3. Cross-case analysis

Through the aforementioned experiments, it is obvious that the functionality of thus-prepared coatings is dependent on both the temperature and time of annealing process, and annealing conditions of 120 °C and 1 h seem to be suitable. However, it is not enough to ascertain that this is the optimal condition for annealing. To fully study the interaction effect of the two independent variables (*i.e.* annealing temperature and time), experiments of more cases were conducted, with 3 temperature cases (120 °C, 130 °C, 140 °C) and 5 time cases (15 min, 30 min, 1 h, 2 h, 4 h) crossed. The results are illustrated in Fig. 10. For all annealing temperature cases, the piezoelectricity of annealed samples shows saturation after a certain annealing time. But when the annealing temperature increases, the required time to reach saturation decreases. For annealing temperature of 130 °C and 140 °C, 30 min is enough, which is shorter than the 1 h at 120 °C. Once reached the saturation, piezoelectric constant values of different annealing temperature cases are close, and remain standing with longer annealing time. Such results implied multiple annealing conditions exist for optimal functionality of thus-prepared PVDF-TrFE coatings, providing a possible explanation for the divergence of observed results among previous studies, *e.g.* 15 min at 135 °C [12] and 1 h at 100 °C [9]. The difference in exact values is probably due to different fabrication methods and film thickness.

## 3.2. Corona poling treatment

Proper annealing treatment can increase the crystallinity of piezopolymer to a high level, which guarantees sufficient dipoles

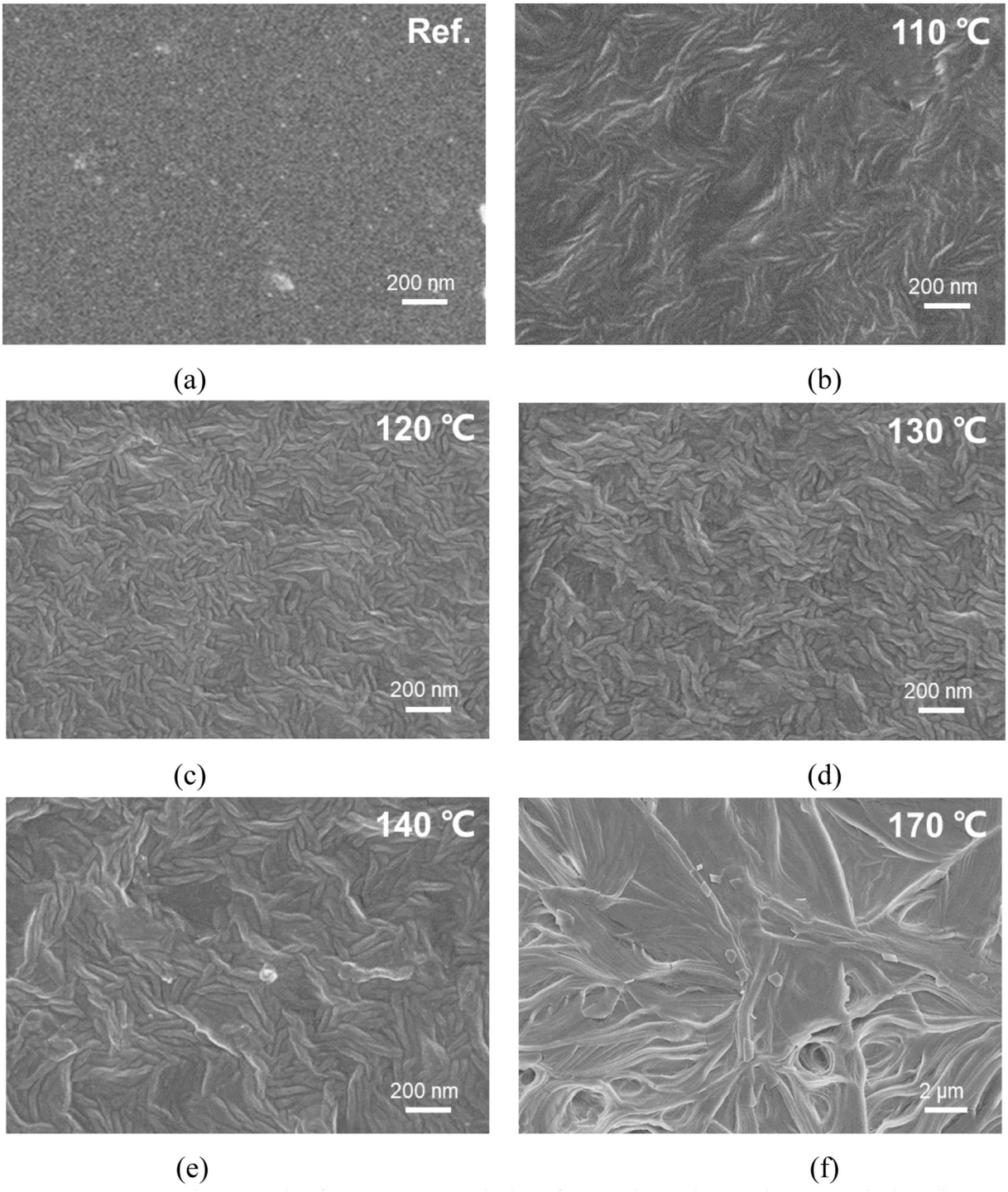


**Fig. 7.** FESEM micrographs for (a) unannealed Ref. sample and samples annealed at (b) 110 °C, (c) 120 °C, (d) 130 °C, (e) 140 °C and (f) 170 °C for 2 h.

in ferroelectric phase to be aligned for polarization by a strong electric field. Corona poling is chosen to be the poling method due to the convenient operation as non-contact and in-air process, which is suitable for the *in-situ* functionalization investigated in this study. The mobile poling pattern introduced (meandering path determined by effective static poling range) also can cover plenty of areas on engineering structures for large-scale SHM applications, with other poling conditions to be investigated. The poling effect is determined by the electrical field and the duration time applied on coatings, which are simultaneously influenced by the voltage on the needle and cycle number in the proposed dynamic *in-situ* poling process. Thus, for parameter study of the poling condition, the poling voltage and cycle were used instead, which can be controlled and compared directly. Piezoelectricity is used to calibrate the poling effect with different conditions. Similarly, each variable is tested individually by fixing the other. To exclude error caused by non-uniformly treated samples, at least three different locations of an individual sample were measured by the proposed piezoelectricity characterization method and results were statistically integrated.

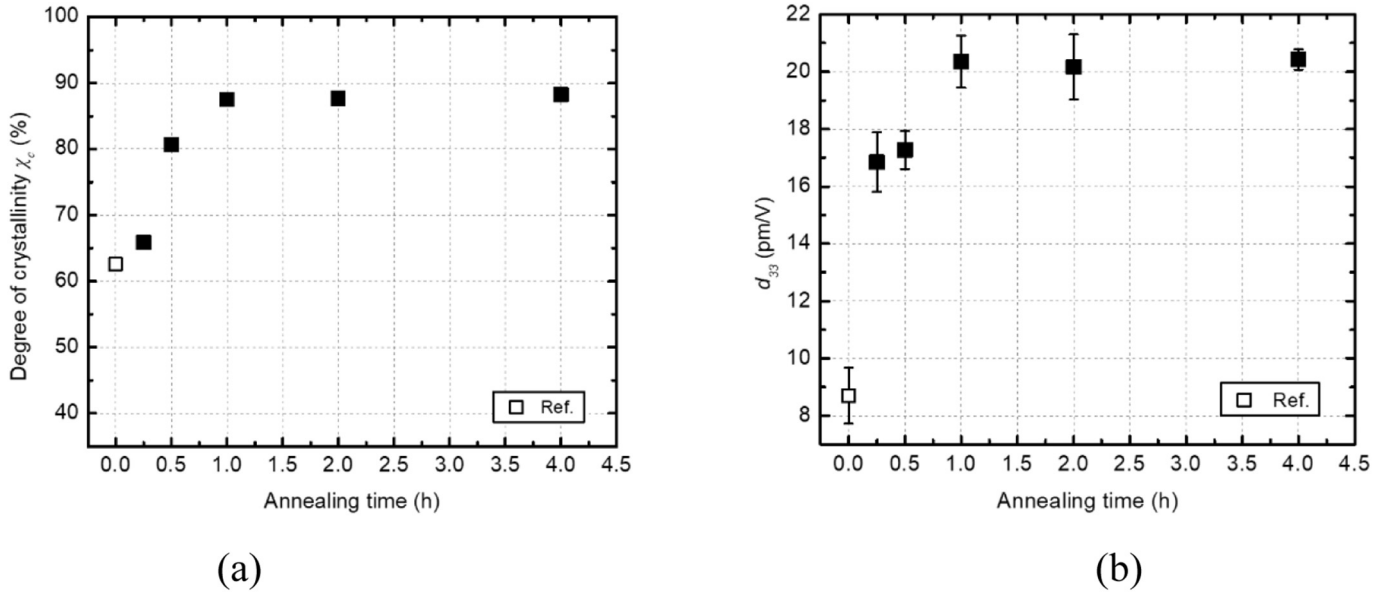


**Fig. 8.** Results of (a) calculated degree of crystallinity and (b) measured piezoelectric constant $d_{33}$ after poling treatment for different annealing time of PVDF-TrFE coatings annealed at 120 °C.

*3.2.1. Poling voltage*

The poling voltage was varied as 15 kV, 20 kV, 25 kV, 30 kV, 35 kV, and 40 kV, with the poling duration set as 10 cycles. The poling temperature was fixed at room temperature. As illustrated in Fig. 11a, the piezoelectricity of poled PVDF-TrFE coatings increases steadily with increasing poling voltage. After poling voltage increased above 35 kV, no obvious improvement of piezoelectricity was observed, and multiple electric arc strikes happened during poling process. The coatings were impaired and broke down, as shown in Fig. 11b. Within the dark boundary (a sign of electrical burn), the substrate which is previously covered by PVDF-TrFE coatings is now clearly visible. An increased electric field will generate more charged ions that can be collected on piezopolymer surfaces, however, too strong electric field will also impair the coatings and increase the breakdown risk.

*3.2.2. Poling duration*

According to the poling voltage results discussed above, the poling duration was controlled as 2 cycles, 5 cycles, 8 cycles, 10 cycles, and 13 cycles with poling voltage of 35 kV, to study the poling duration effect on the functionality of treated coatings. Fig. 12 shows the experimental results, where the duration of 5 cycles exhibits the highest piezoelectricity. It seems that there is an optimal duration, shorter than which would result in incomplete poling treatment while longer than which would overcharge the piezopolymer coatings and impair the functionality.

*3.2.3. Cross-case analysis*

Similarly, previous experimental results are not sufficient to fully investigate the poling condition, considering the interaction between the poling voltage and duration. Accordingly, experiments of more cases were conducted, with 4 voltage cases (20 kV, 25 kV, 30 kV, 35 kV) and 4 duration cases (2 cycles, 5 cycles, 8 cycles, 10 cycles) crossed. As shown in Fig. 13, the increased poling voltage would reduce the required poling duration to reach the highest piezoelectricity value. For example, at 25 kV, the highest piezoelectricity is obtained with 8 cycles, while similar highest piezoelectricity value is reached at 35 kV for 5 cycles. The fall of piezoelectricity value after peak value suggests that excessive poling has an adverse effect on the functionality of piezopolymer coatings. These results indicate that multiple optimal poling conditions exist, considering that the poling voltage and poling cycle contribute synergistically to the accumulated charges on the surface of piezopolymer.

To examine the crystalline change due to the rotation of dipoles after poling process, XRD was performed on samples poled at 35 kV for 5 cycles. The result was compared with unpoled samples as in Fig. 14. The peak of (110) and (200) Bragg reflections becomes stronger and narrower after poling process, with shifting to a slightly higher angle. Moreover, two more diffractions related to ferroelectric phase can be observed, at 35.4° which is attributed to Bragg reflections of (001), (310), (020), and at 40.8° which is attributed to Bragg reflections of (111), (201), (220), (400). These results indicate the increase of crystallinity and reduction of lattice expansion, which can be explained by that the rotation of dipoles under a strong electric field helps perfect the ferroelectric phase by reorientation of the molecular chain and reduction of *gauche* defects [10]. Crystallization and polarization of piezopolymer coatings will enhance each other mutually, leading to the final high level of piezoelectricity.

Since the piezoelectricity is proportional to the amplitude of wave signals captured by piezoelectric-type sensors, based on the multiple processing parameters studied above, the functionalization conditions were set as annealing at 130 °C for 0.5 h, followed by poling at 35 kV for 5 cycles to achieve strong piezoelectricity. The $d_{33}$ of thus-prepared sensors is 20.4 ± 0.6 pm/V with a thickness of 20.3 ± 0.4 μm. The good consistency guarantees the robustness of the following verification experiments including guided wave sensing, actuation, and damage identification.

*3.3. Passive acoustic emission*

As shown in Fig. 4a, the distance between two thus-prepared sensors (SEN-L and SEN-R) is 160 mm. Acoustic source created by lead break will emit elastic guided waves along the structure. Representatively, AE signals from the surface lead break at 120 mm from SEN-L are shown in Fig. 15. The corresponding frequency spectra are obtained through fast Fourier transform. Apparently, the elastic guided waves arrive firstly at the location of SEN-R (Fig. 15a) and the frequency band is below 10 kHz (Fig. 15b). According to the dispersion curves of 2 mm aluminium plate (Fig. 16), the frequency band in this experiment is quite lower than the cut-off frequencies of those high-order wave modes (such as the first- and second-order,

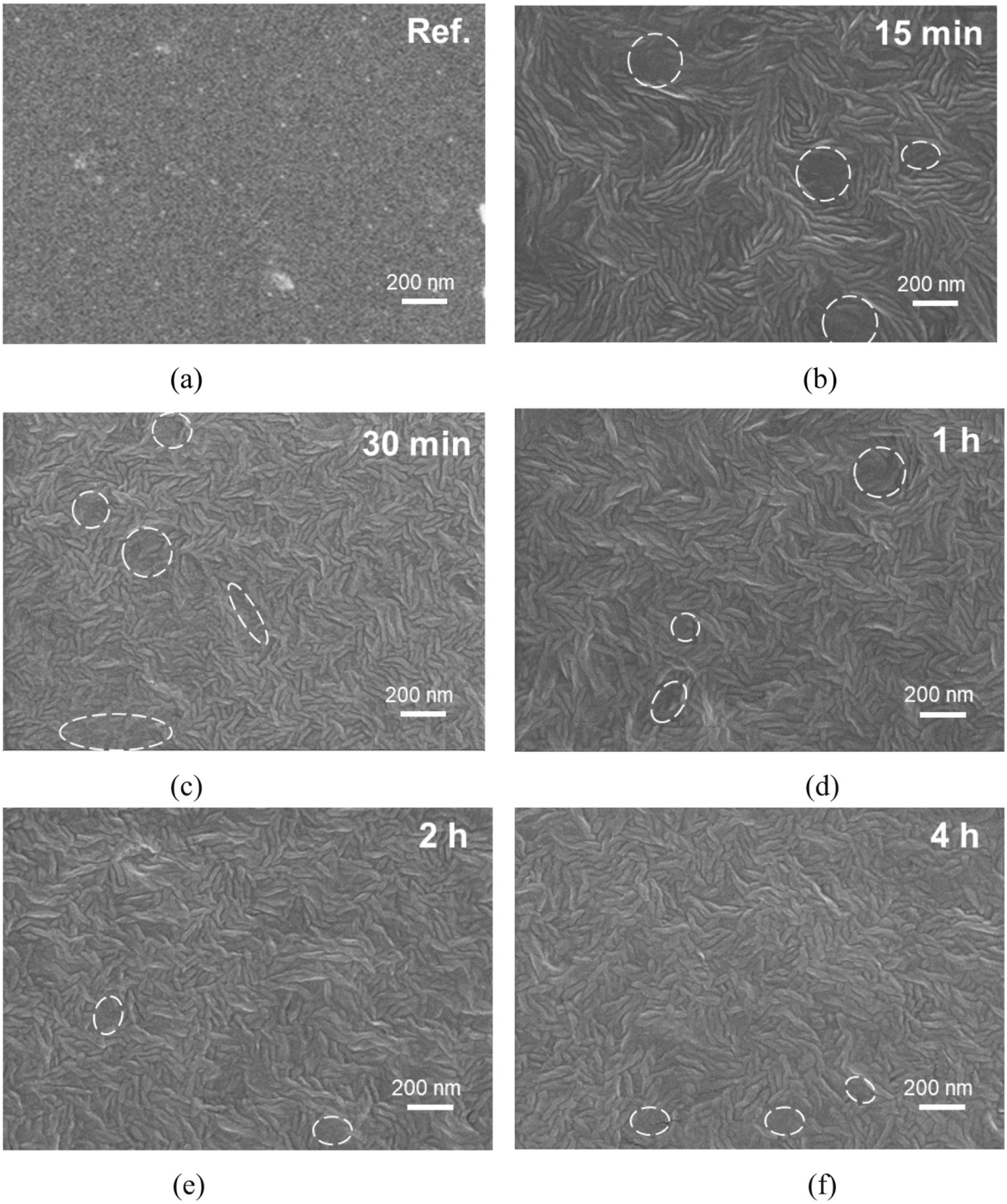


**Fig. 9.** FESEM micrograph for (a) unannealed Ref. samples and samples annealed at 120 °C for (b) 15 min, (c) 30 min, (d) 1 h, (e) 2 h, and (f) 4 h, with non-crystalline domains white circled.

symmetric and anti-symmetric modes, denoted as $S_1$, $S_2$, $A_1$, and $A_2$, respectively, in Fig. 16a). Thus, only fundamental Lamb wave modes exist, *i.e.* the zeroth-order symmetric and anti-symmetric modes ($S_0$ and $A_0$ in Fig. 16). Based on the exhibited dispersive features (the wave velocity varies with frequency), $A_0$ is observed to be the dominant propagating wave mode, which is also in accordance with the out-of-plane excitation.

With obtained wave signals, a *delay-and-sum* imaging algorithm [46] is recalled to locate source spots. With the impact occurring at $(x, y)$, wave signals reach two sensors $a$ $(x_a, y_a)$ and $b$ $(x_b, y_b)$ at time $t_a$ and $t_b$,

$$\begin{aligned} t_a &= t_0 + \Delta t_a \\ t_b &= t_0 + \Delta t_b \end{aligned} \tag{4}$$

where $t_0$ is the moment when a break occurs, and $\Delta t$ is the travelling time for $A_0$ wave mode from source to sensors. The time difference $\Delta t_{ab}$ in the arrival time of $A_0$ captured by sensor a and b yields

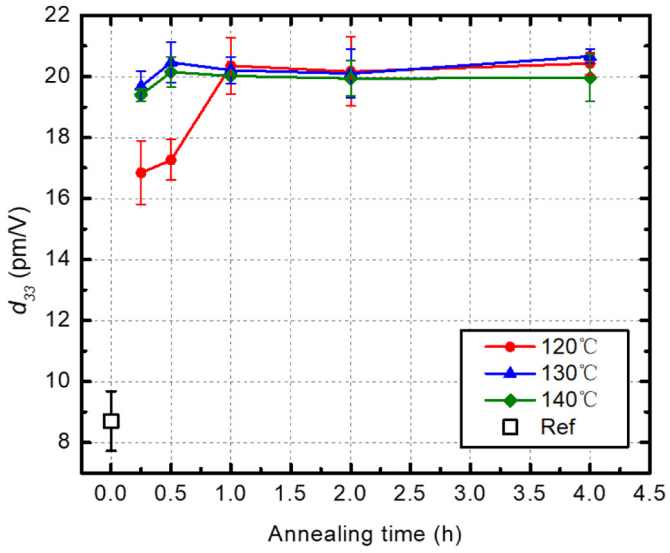


**Fig. 10.** Piezoelectricity results of PVDF-TrFE coatings with two variables - annealing time and temperature - crossed.

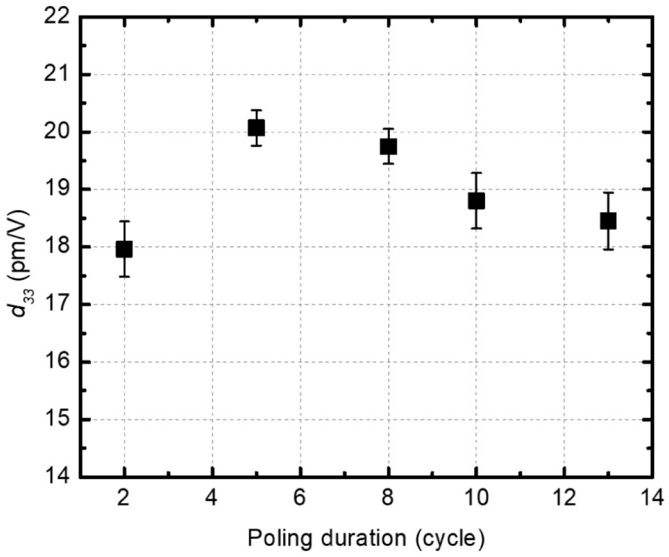


**Fig. 12.** Piezoelectricity results of PVDF-TrFE coatings *versus* poling cycles.

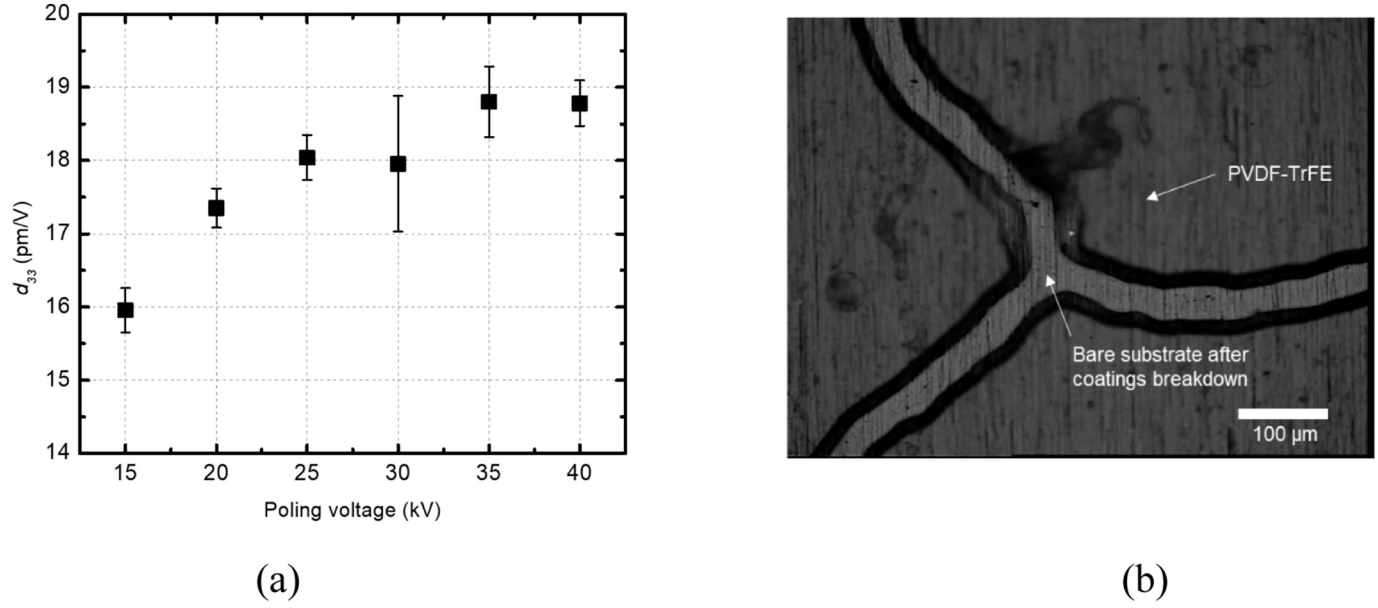


**Fig. 11.** (a) Piezoelectricity results of PVDF-TrFE coatings *versus* poling voltages; (b) typical breakdown spot when poled at 40 kV.

$$\Delta t_{ab}(x,y) = t_a - t_b = (t_0 + \Delta t_a) - (t_0 + \Delta t_b) = \frac{\sqrt{(x-x_a)^2 + (y-x_a)^2} - \sqrt{(x-x_b)^2 + (y-x_b)^2}}{v_{wave}}, \quad (5)$$

where $v_{wave}$ is the wave velocity derived from either theoretic dispersion curves or experiments. Since in this experiment two sensors were used on a beam, the location of acoustic source could be imaged using a one-dimensional probability-based diagnostic imaging tomography [47] with its pixel value defined as

$$I_{ab}(x) = \max\left(E_a + E_b(\Delta t_{ab}(x))\right), \quad (6)$$

where $E$ is the energy packet of $A_0$ mode obtained using a wavelet transform [48]. The signals at sensors a and b are delayed and summed accordingly and the maximum value of the summation results can be linked to the probability of occurrence of an acoustic source. The image result derived from signals in Fig. 15 is depicted in Fig. 17, from which it is clear to observe that the real break spot matches well with the highlighted diagnostic area, which represents the calculated most probable source location. This method can be extended to a two-dimensional image with multiple sensing paths applied for more precise evaluation, and used for identification of impact location.

The in-plane excitation was performed by lead breaking on the right edge of the specimen, as illustrated in Fig. 4. A low-noise preamplifier (Stanford Research Systems SR560) was used to amplify captured signals due to the low-level amplitude. As shown in Fig. 18, the wave packets arrive firstly at SEN-R and the frequency band (<40 kHz) is higher than AE signals of the surface break. However, the first wave

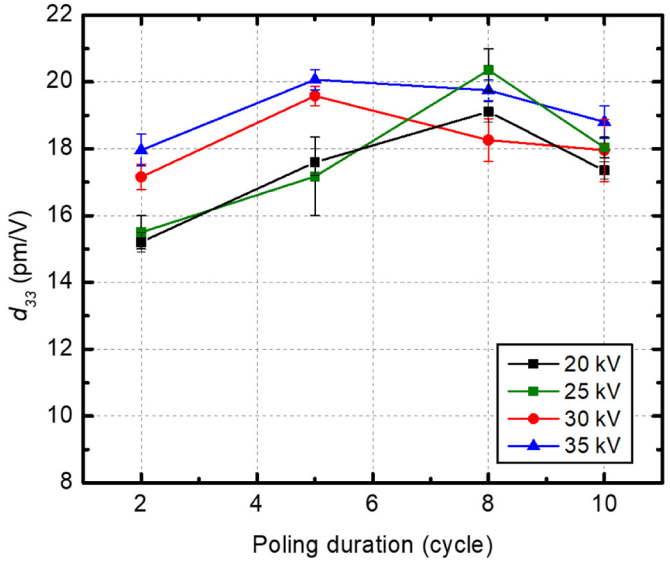


**Fig. 13.** Piezoelectricity results of PVDF-TrFE coatings with two variables - poling duration and temperature - crossed.

packets arrive at SEN-L seemed to be the overlap of multiple waves, probably caused by the reflection of narrow boundaries in the beam specimen. Thus, the leading edge is used to identify the time delay, as 30.6 μs. Considering the distance between two sensors, the calculated wave velocity is 5228 m/s, which was close to the wave velocity of $S_0$ mode (5343 m/s in Fig. 16b), in accordance with the in-plane source simulation.

### 3.4. Active ultrasonic transmission

A pitch-catch ultrasonic transmission was performed, with two four-finger comb electrodes (155 mm distance) painted on the PVDF-TrFE coatings on the inspected beam specimen. The comb electrodes are proven to be effective for exciting specific frequency-mode guided waves *via* controlling the finger gap [49]. The finger gap should be equal to half wavelength of pre-selected guided waves, determined with the help of dispersion curves (Fig. 19). In this study, with the same wavelength of 6.6 mm, $A_0$ mode at 300 kHz and $S_0$ mode at 770 Hz were excited and compared. Both pre-selected frequencies are in the low-frequency region where only two fundamental zeroth-order Lamb wave modes exist, *i.e.* $S_0$ and $A_0$.

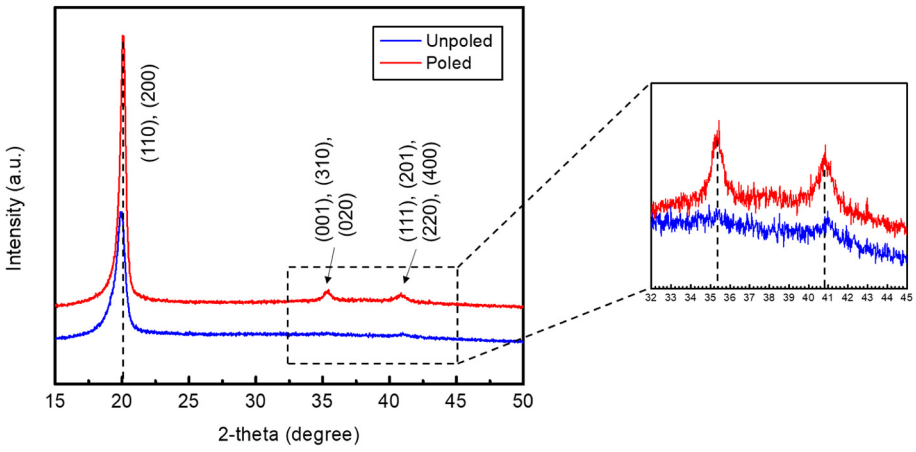


**Fig. 14.** Comparison of XRD results of unpoled and poled PVDF-TrFE coatings.

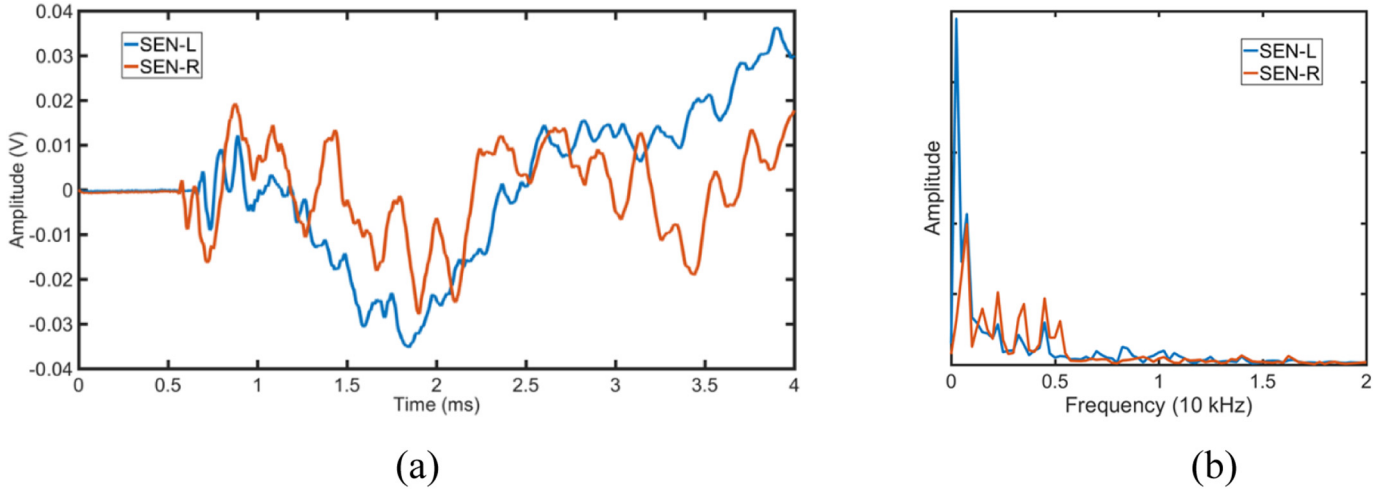


**Fig. 15.** AE signals from surface lead break (a) in the time domain and (b) in the frequency domain.

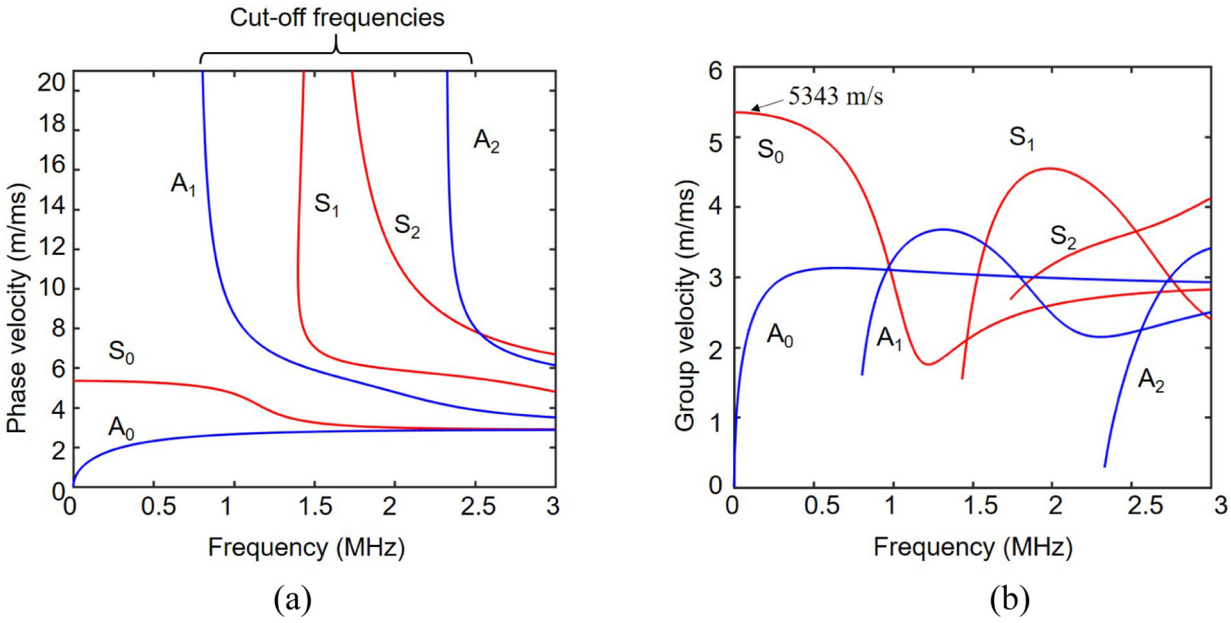


**Fig. 16.** Guided wave theoretical dispersion curves of 2 mm aluminium plate with multiple high-order modes (a) phase velocity and (b) group velocity.

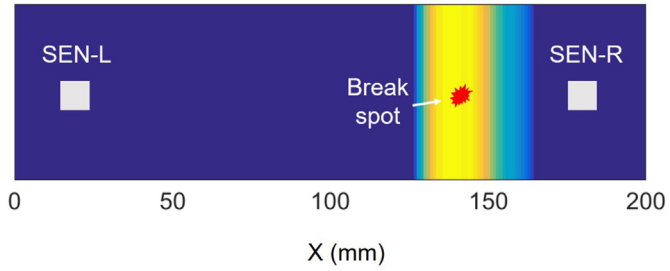


**Fig. 17.** Comparison between identified and real acoustic source of lead break.

6-cycle Hanning-function-modulated sinusoidal tone bursts were used to excite guided waves propagating in the specimen from Actuator in Fig. 4b. The captured baseline signals (intact status without artificial defect) by Sensor in Fig. 4b at 300 kHz are illustrated in Fig. 20b. The time of flight (ToF) is determined by the energy envelope curve obtained using the Hilbert transform. With known distance, the calculated group velocities of first-arrived $S_0$ mode and $A_0$ mode are 2.95 and 4.46 m/ms, respectively. These values are close to the theoretical results (2.97 and 4.41 m/ms) labeled in Fig. 19b. The mass block was attached in the middle of the Actuator and Sensor by couplant as an artificial defect, and the current signals are illustrated in Fig. 20c. $A_0$ mode is observed to be the predominant wave packets at 300 kHz, with significantly weaker $S_0$ mode before it. Comparing the baseline and current signals, it is easy to notice the decreasing amplitude of $A_0$ wave packets from 35 mV to 21 mV, a phenomenon known as attenuation, due to the wave energy dissipation after passing through the defect. Fig. 21 is the signals captured at 770 kHz. The $S_0$ mode here is only slightly stronger than $A_0$ mode, and the amplitude of $S_0$ wave packets in baseline and current signals decreases from 15.4 mV to 13.3 mV. Although $A_0$ at 300 kHz and $S_0$ at 770 kHz are both matching the wavelength pre-selected, the efficiency of wave mode filtering and damage identification is quite different. As shown in Fig. 22a, the ratios of pre-selected fundamental zeroth-order wave mode *versus* the other fundamental

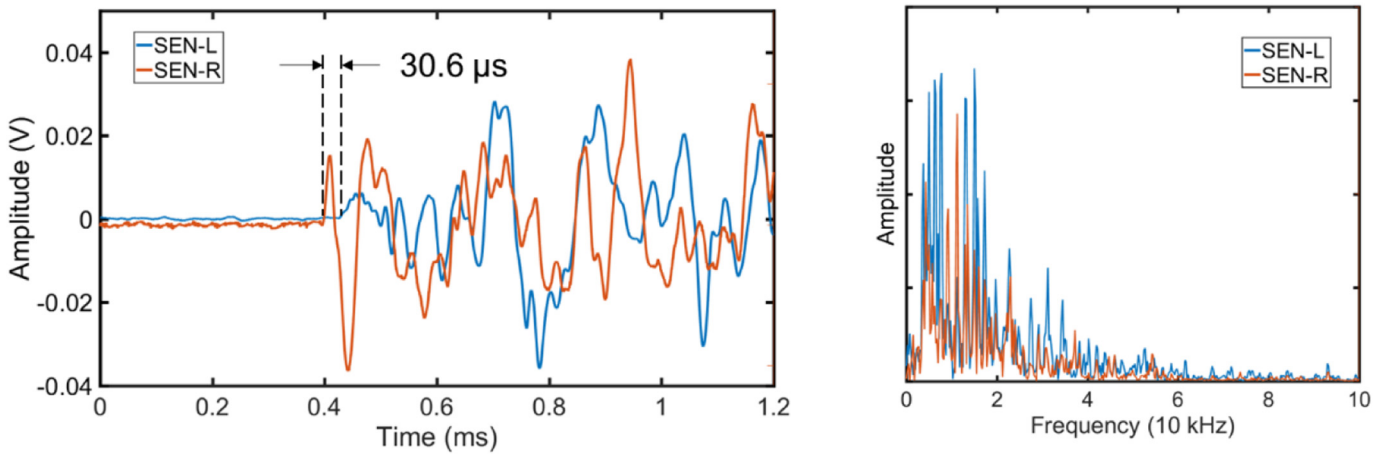


**Fig. 18.** AE signals from edge lead break (a) in the time domain and (b) in the frequency domain.

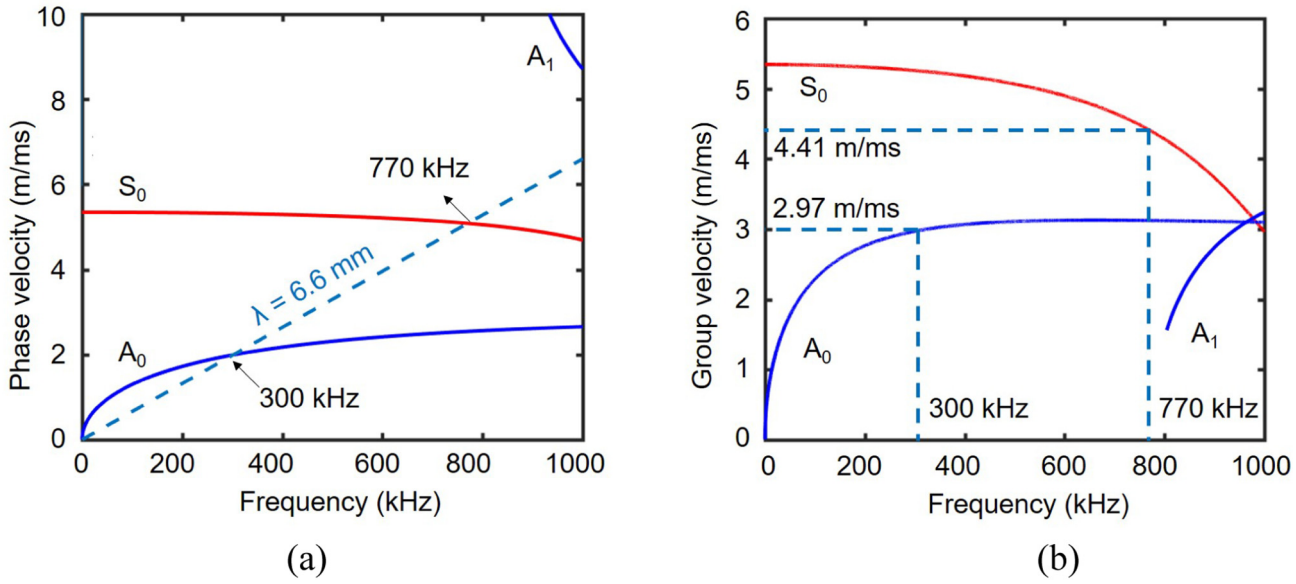


**Fig. 19.** (a) Corresponding wave modes and frequencies of pre-selected wavelength and (b) group velocity of corresponding wave modes and frequencies.

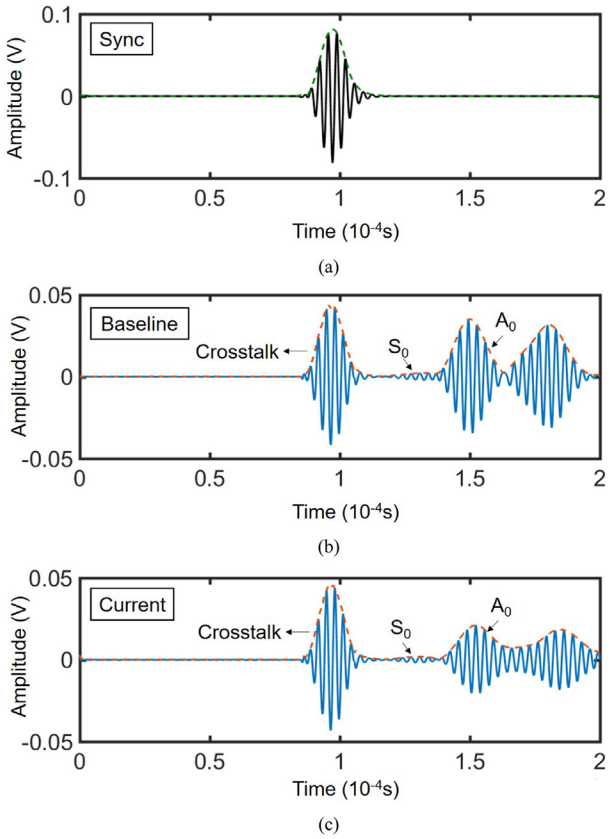


**Fig. 20.** Excitation of 300 kHz: (a) sync signals from wave generator; (b) baseline signals captured by Sensor; (c) current signals captured by Sensor.

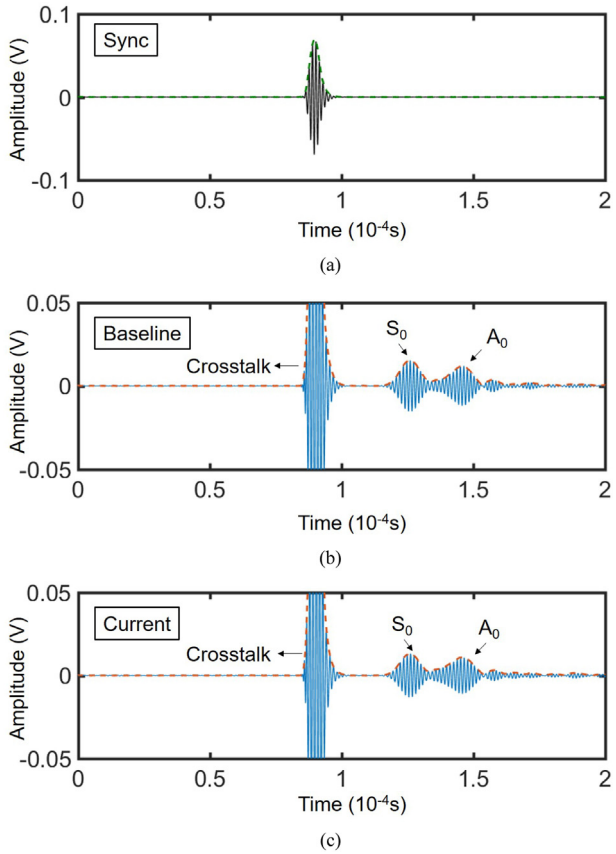


**Fig. 21.** Excitation of 770 kHz: (a) sync signals from wave generator; (b) baseline signals captured by Sensor; (c) current signals captured by Sensor.

zeroth-order wave mode are 14.96 for $A_0/S_0$ at 300 kHz and 1.28 for $S_0/A_0$ at 770 kHz. Generally, the first predominant wave packets are used as the diagnostic signals to identify the defect, to avoid interference from boundary-reflected waves [50]. In this case, diagnostic signals are selected as $A_0$ at 300 kHz and $S_0$ at 770 kHz. The attenuation of the diagnostic signal is chosen as the feature of received signals to be extracted for constructing *damage index* (*DI*) as

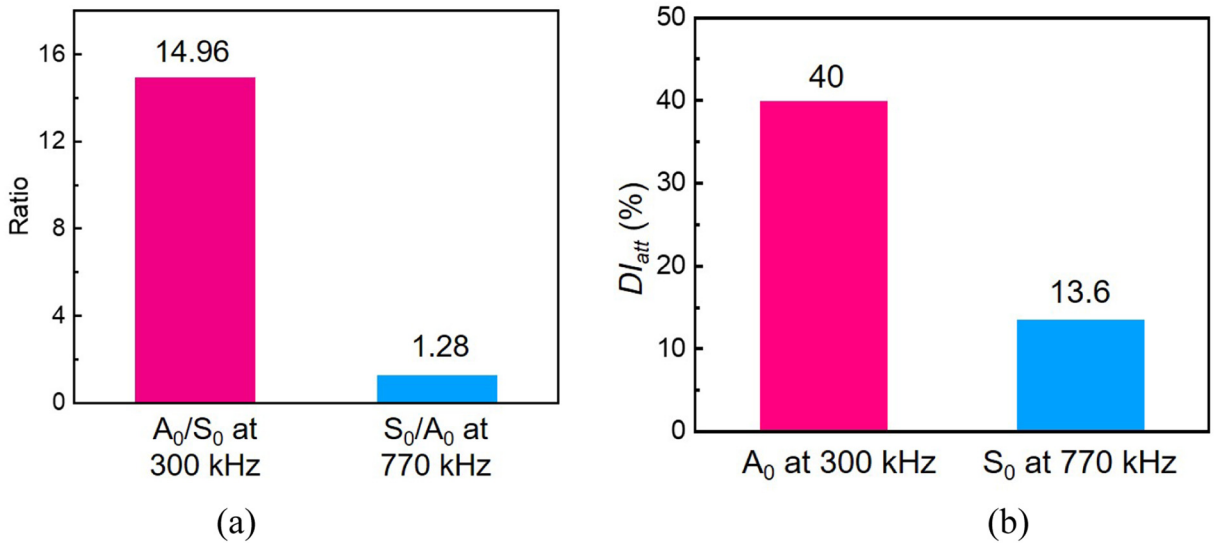


**Fig. 22.** (a) The ratios of pre-selected wave mode *versus* the other; (b) the attenuation-based damage index of pre-selected diagnostic signals.

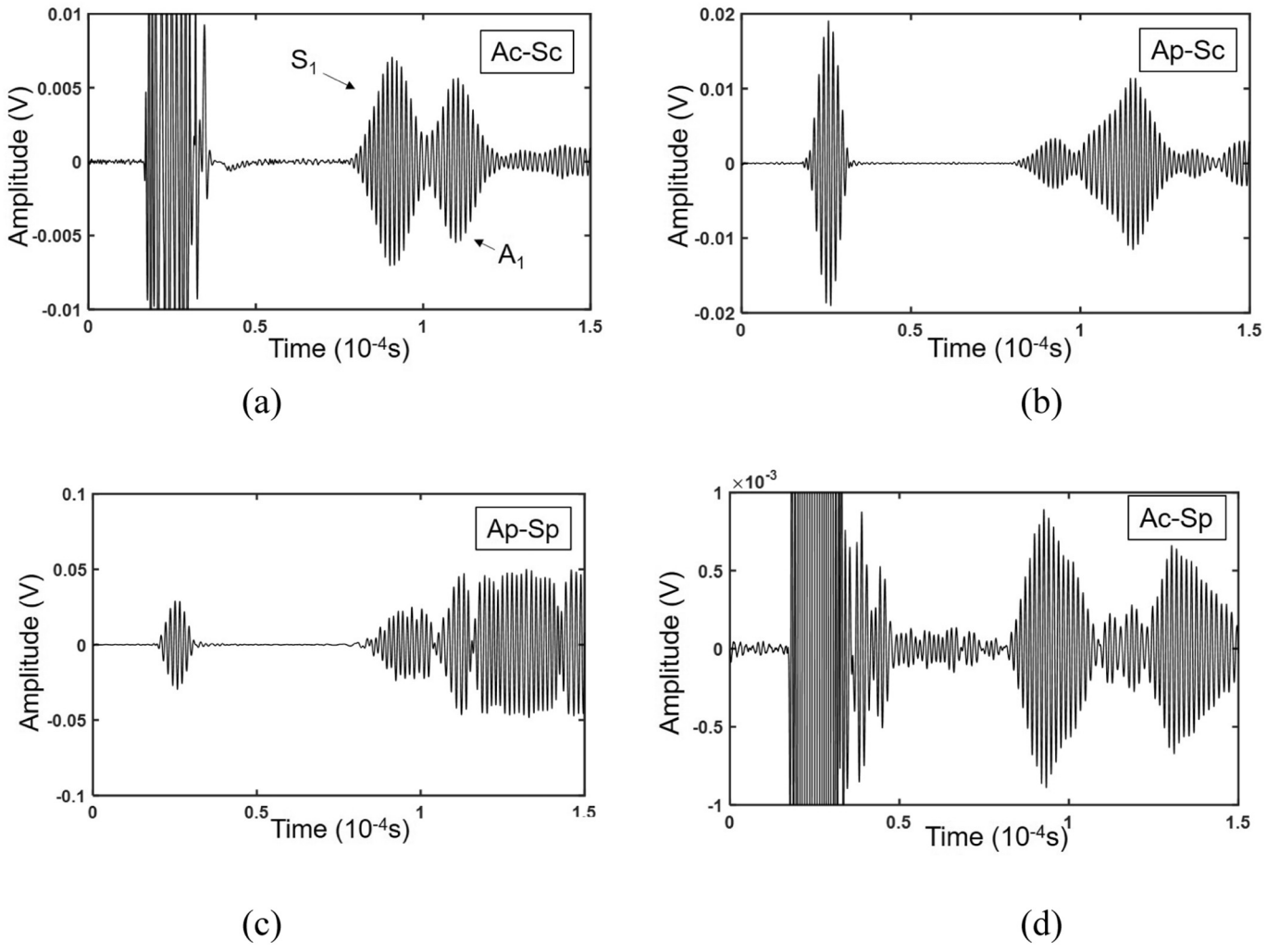


**Fig. 23.** Wave signals of sensing paths with different actuator and sensor (a) $A_c$-$S_c$; (b) $A_p$-$S_c$; (c) $A_p$-$S_p$; (d) $A_c$-$S_p$.

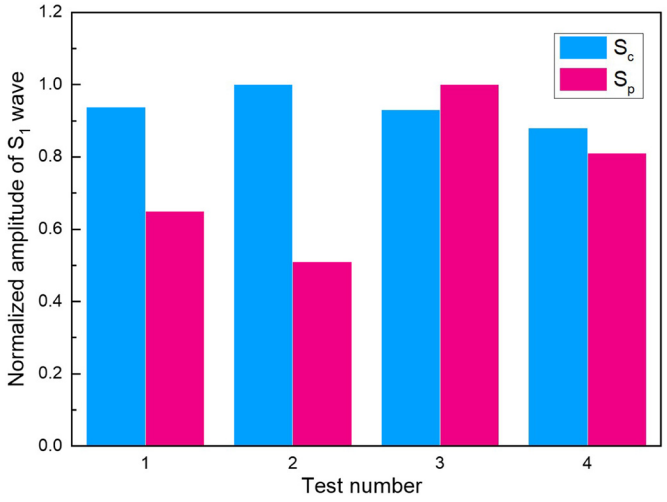


**Fig. 24.** Normalized amplitude of $S_1$ wave captured by $S_p$ and $S_c$.

$$DI_{att} = \frac{|E_{current} - E_{baseline}|}{E_{baseline}}, \quad (7)$$

where $E_{current}$ and $E_{baseline}$ is the amplitude of diagnostic wave energy determined by Hilbert transform of current and baseline signals, respectively. The calculated $DI_{att}$ are 40% for $A_0$ at 300 kHz and 13.6% for $S_0$ at 770 kHz, as in Fig. 22b. Such relatively higher attenuation of the $A_0$ wave packets after surface-attached mass is caused by the dominant out-of-plane displacement of particles of $A_0$ mode, which makes the wave energy easier to be leaked to the surface and more sensitive to the surface defect, comparing to the $S_0$ mode which mostly has in-plane displacement. Thus, for comb electrode form and pitch-catch wave transmission method in this study, $A_0$ mode is more efficient to be solely excited, and more effective to be the active diagnostic signals for additional mass identification. The mass block were moved to other locations on the sensing path, and similar results were obtained. The crosstalk at the initial time in all received signals is attributed to spatial electromagnetic interference (EMI) from the high-voltage power amplifier during wave generation [51].

### 3.5. Piezopolymer coatings vs. surface-mounted PZTs

To further evaluate the performance of piezopolymer coatings, they were used to actuate and sense high-order Lamb wave modes with comparison of conventional PZT wafers. Piezopolymer coatings were fabricated on a 5 mm aluminium plate. $S_1$ wave mode was selected as the diagnosis signal with frequency-thickness product of 3.52 MHz·mm, the phase velocity of which equalled to that of longitudinal wave, being a typical fundamental wave selection in nonlinear ultrasonics. Comb electrodes were printed with dimensions matching the wavelength ($\lambda$ = 8.38 mm). Commercial PZT discs (diameter of 9 mm and thickness of 1 mm) were manually attached to the opposite side of the plate at the same location using instant glue. The actuators were excited by 10-cycle Hanning-function-modulated tone bursts with a voltage of 50 V for PZT and 250 V for piezopolymer coatings, due to the differences in piezoelectricity, and the ultrasonic signals received by the sensors were amplified and analyzed. The actuator and sensor of piezopolymer coatings and PZTs were denoted as $A_c$, $S_c$ and $A_p$, $S_p$, respectively, shown in Fig. 23. PZT wafers have "tuning effect" when actuating and sensing ultrasonic signals, which requires their dimensions to be selected prior to installation. The wavelength mismatch of PZT wafers would result in low actuation and sensing efficiency, and may be a problem for high-frequency region, where multiple modes exist. In this experiment, the PZT wafers had a diameter close to the wavelength, being in the condition of poor wavelength match. Thus, as shown in Fig. 23b, c and d, the multi-mode nature of Lamb wave resulted in superposition of multiple waveforms, inducing difficulties in feature recognition and signal processing. For proposed piezopolymer coatings, the dimensions of electrodes can be adaptive and *in-situ* adjusted conveniently, which could

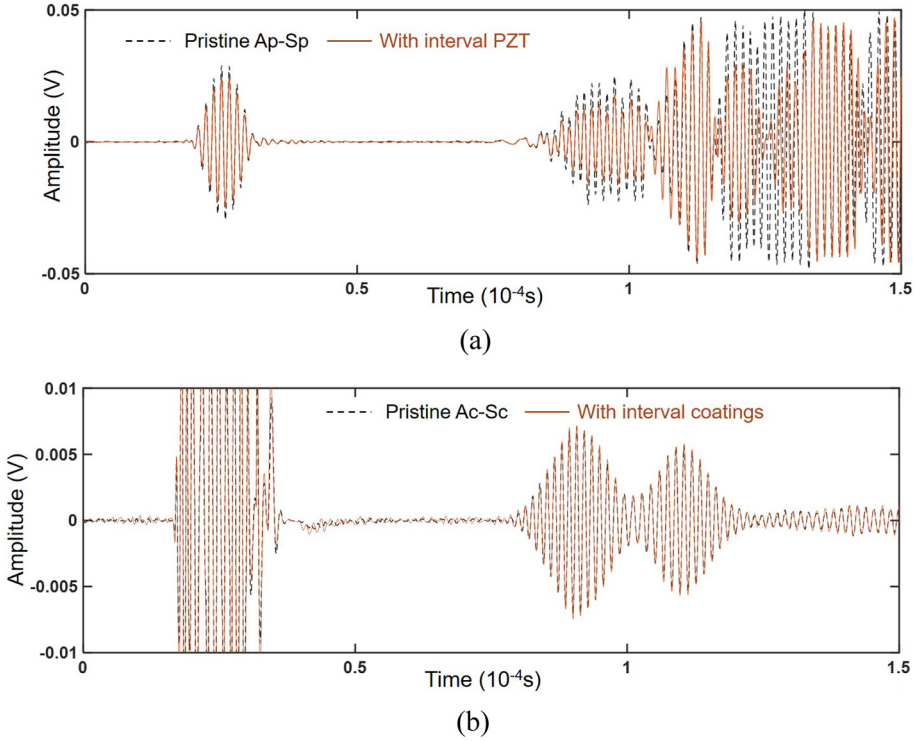


**Fig. 25.** The signal difference caused by one additional sensor placed in the sensing path of (a) PZTs; (b) coatings.

precisely match the wavelength of required diagnosis signals and also enhance the required waveforms by multiple fingers. Thus, although the $A_1$ mode is also predominant in Fig. 23a due to the close wavelength, the $A_c$-$P_c$ combination provides the most distinct $S_1$ mode waveform. The high adaptability of sensors made of piezopolymer coatings provides possibility as permanently installed SHM networks for advanced diagnosis methods in multi-mode region, for example nonlinear ultrasonics, in which the transducer/wedge assembly is most commonly used to obtain required diagnosis signals. However, it should be noticed that, even under low excitation efficiency, the PZT pair $A_p$-$S_p$ can still excite $S_1$ mode with amplitude of 22 mV (Fig. 23c), while the piezopolymer coatings pair $A_c$-$P_c$ obtains about 7 mV $S_1$ mode with 5 times excitation voltage (Fig. 23a). This is caused by the relatively lower piezoelectricity of piezopolymer, and may cause problems for acquiring effective signals in some applications, for example, high attenuation materials or long wave propagation distance.

To evaluate the consistency of sensors, four different individuals of PZT wafers and piezopolymer coatings at same distance were examined by the amplitude of the first-arrived $S_1$ wave packet. Manually installed PZT wafers would suffer from the variation of bonding quality and thickness [52], which yields poor consistency, as shown in Fig. 24. On the other hand, the automated *in-situ* manufactured coatings achieve more consistent performance with standard deviation of 0.05.

Another major difference investigated is the inter-path interference of sensors on wave propagation. Considering the sizable dimensions and mass, PZT wafers would cause diffraction of waves when propagating through, which is difficult to distinguish from real defects, as shown in Fig. 25a. Thus, when designing sensing networks, PZT wafers are usually located in the perimeter of the inspected area, and the sensing path should avoid interaction with interval sensors. On the other hand, the low profile and light weight of piezopolymer coatings would barely perturb the local stiffness to cause wave diffraction (Fig. 25b), which provides more possibility and flexibility in designing sensing networks for SHM.

## 4. Concluding remarks

PVDF-TrFE coatings were successfully *in-situ* fabricated and functionalized on structures *via* an automated multiple-step process including spray, annealing, and poling. Processing conditions were systematically examined and interacted to study their influence on crystallization and piezoelectricity of thus-prepared piezopolymer coatings. Results indicated that the improvement of crystallization and piezoelectricity required annealing temperature to be between $T_c$ and $T_m$, and had a threshold value which can be reached after a certain time, generally shorter with higher temperature, *e.g.* 1 h at 120 °C and 30 min at 140 °C. This conclusion partially resolved the discrepancies in previous studies by different groups. For corona poling, the applied electrical voltage had a proper range for polarization, while the duration was important to obtain the best polarization effect. Results indicated that with a strong electric field, short duration could be expected (5 cycles at 35 kV). The annealing process improves the crystallization of the ferroelectric phase within PVDF-TrFE, which positively affects the polarization in poling process, *i.e.* more dipoles available for rotation. In turn, the poling process could further enhance the ferroelectric phase, through reducing the *gauche* defects. Through such a systematic and comprehensive study, the pattern of the correlation between multiple processing conditions and functional properties of piezopolymer coatings became distinct, and the suitable conditions of optimal functional performance were identified and rationalized. These results are particularly interesting for large-scale industrial applications where time and energy efficiency are highly valued.

To validate the functionality and feasibility of thus-prepared piezopolymer coatings as sensors to be networked in SHM, guided waves were used as diagnostic signals to be captured and activated *via* a series of tests. In passive AE experiment, with monolithic electrodes, PVDF-TrFE coatings can be used to capture broadband and multi-mode wave signals for source localization. In active ultrasonic transmission, by corresponding the finger gap of comb electrodes with the wavelength, the pre-selected narrowband frequency-mode guided wave signals can be tuned for defect identification. Results indicated that thus-prepared piezopolymer coatings were fully functional for sensing and actuation purposes in a wide frequency range. Damage-related features could be easily identified and used for damage quantification. The adaptability to tune specific frequency-mode waves, the high consistency of different individuals, and negligible inter-path interference to wave propagation provide possibility for designing novel sensing networks of high density and completeness with minimal penalty. However, the low piezoelectricity of piezopolymer could limit its applications due to low wave transducing efficiency, compared to piezoceramics. The development of strong piezoelectric coatings could be a solution, through functional modification of piezopolymer or new materials. Authors are also working on improving the piezoelectricity of PVDF-TrFE coatings through introducing nanoparticles.

The *in-situ* fabrication and functionalization method in this study, realized by moving different functional processing heads over the to-be-inspected area on structures, although without shear force in spin coating or self-polarized and stretched in electrospinning, can result in piezopolymer coatings with good functional properties by proper processing treatments. Moreover, automated processes minimize the impact of human factors during fixing and aligning of conventional sensors and improve the consistency and reproducibility of functional performance. Furthermore, rapid prototyping of sensing networks directly formed on inspected structures is suitable for continuous and mass production.

The proposed sensing networks of piezopolymer coatings possess many advantages over conventional installed networks, including ultra-light weight, ultra-low profile, flexibility and adhesive-free attachment. There features enable high adaptability, high consistency, and negligible inter-path interference in wave actuation and sensing. *In-situ* manufactured piezopolymer coatings could introduce novelty and creativity to design sensing networks for complex structures, and potential for health monitoring on more extended applications like soft bio-organic parts and pouch battery cells. The integration of such sensing networks and advanced SHM technology to detect various types of damage on different structures will be delivered in future work.

## Declaration of Competing Interest

The authors declare that they have no known competing financial interests or personal relationships that could have appeared to influence the work reported in this paper.

## Acknowledgments

This project is supported by National Natural Science Foundation of China (Grant No. 52005493) and China Postdoctoral Science Foundation (Grant No. 2020M682979). The authors are also grateful to the financial support from the Science and Technology Innovation Commission of Shenzhen (No. ZDSYS20190902093209795, No. JCYJ20170818153048647 and No. JCYJ20180507182239617).

## References

[1] M. Mitra, S. Gopalakrishnan, Guided wave based structural health monitoring: a review, Smart Mater. Struct. 25 (2016) 053001.
[2] H. Mei, M.F. Haider, R. Joseph, A. Migot, V. Giurgiutiu, Recent advances in piezoelectric wafer active sensors for structural health monitoring applications, Sensors. 19 (2019) 383.
[3] Z. Su, L. Ye, Lamb wave propagation-based damage identification for quasi-isotropic CF/EP composite laminates using artificial neural algorithm: part II - implementation and validation, J. Intell. Mater. Syst. Struct. 16 (2005) 113–125.
[4] Y. Ting, Suprapto, C.-W. Chiu, H. Gunawan, Characteristic analysis of biaxially stretched PVDF thin films, J. Appl. Polym. Sci. 135 (2018) 46677.

[5] P. Viswanath, K.K.H. De Silva, H.-H. Huang, M. Yoshimura, Large piezoresponse in ultrathin organic ferroelectric nano lamellae through self-assembly processing, Appl. Surf. Sci. 532 (2020) 147188.
[6] E. Bellet-Amalric, J.F. Legrand, Crystalline structures and phase transition of the ferroelectric P(VDF-TrFE) copolymers, a neutron diffraction study, Eur. Phys. J. B. 3 (1998) 225–236.
[7] Y.J. Park, S.J. Kang, C. Park, K.J. Kim, H.S. Lee, M.S. Lee, et al., Irreversible extinction of ferroelectric polarization in P(VDF-TrFE) thin films upon melting and recrystallization, Appl. Phys. Lett. 88 (2006).
[8] D. Mao, M.A. Quevedo-Lopez, H. Stiegler, B.E. Gnade, H.N. Alshareef, Optimization of poly(vinylidene fluoride-trifluoroethylene) films as non-volatile memory for flexible electronics, Org. Electron. 11 (2010) 925–932.
[9] R.I. Mahdi, W.C. Gan, W.H.A. Majid, Hot plate annealing at a low temperature of a thin ferroelectric P(VDF-TrFE) film with an improved crystalline structure for sensors and actuators, Sensors. 14 (2014) 19115–19127.
[10] C.Y.B. Ng, W.C. Gan, T.S. Velayutham, B.T. Goh, R. Hashim, Structural control of the dielectric, pyroelectric and ferroelectric properties of poly(vinylidene fluoride-co-trifluoroethylene) thin films, Phys. Chem. Chem. Phys. 22 (2020) 2414–2423.
[11] M. Baniasadi, Z. Xu, J. Cai, S. Daryadel, M. Quevedo-Lopez, M. Naraghi, et al., Correlation of annealing temperature, morphology, and electro-mechanical properties of electrospun piezoelectric nanofibers, Polymer. 127 (2017) 192–202.
[12] N. Spampinato, J. Maiz, G. Portale, M. Maglione, G. Hadziioannou, E. Pavlopoulou, Enhancing the ferroelectric performance of P(VDF-co-TrFE) through modulation of crystallinity and polymorphism, Polymer. 149 (2018) 66–72.
[13] D. Zhao, I. Katsouras, K. Asadi, P.W.M. Blom, D.M. de Leeuw, Switching dynamics in ferroelectric P(VDF-TrFE) thin films, Phys. Rev. B 92 (2015) 214115.
[14] A. Aliane, M. Benwadih, B. Bouthinon, R. Coppard, F. Domingues-Dos Santos, A. Daami, Impact of crystallization on ferro-, piezo- and pyro-electric characteristics in thin film P(VDF–TrFE), Org. Electron. 25 (2015) 92–98.
[15] W. Li, Y. Zhu, D. Hua, P. Wang, X. Chen, J. Shen, Crystalline morphologies of P(VDF-TrFE) (70/30) copolymer films above melting point, Appl. Surf. Sci. 254 (2008) 7321–7325.
[16] Z. Fu, W. Xia, W. Chen, J. Weng, J. Zhang, J. Zhang, et al., Improved thermal stability of ferroelectric phase in epitaxially grown P(VDF-TrFE) thin films, Macromolecules. 49 (2016) 3818–3825.
[17] F. Xia, B. Razavi, H. Xu, Z.-Y. Cheng, Q.M. Zhang, Dependence of threshold thickness of crystallization and film morphology on film processing conditions in poly(vinylidene fluoride–trifluoroethylene) copolymer thin films, J. Appl. Phys. 92 (2002) 3111–3115.
[18] A.J. Lovinger, G.E. Johnson, H.E. Bair, E.W. Anderson, Structural, dielectric, and thermal investigation of the curie transition in a tetrafluoroethylene copolymer of vinylidene fluoride, J. Appl. Phys. 56 (1984) 2412–2418.
[19] K. Kap Jin, Bum K. Gwan, Curie transition, ferroelectric crystal structure and ferroelectricity of a VDF/TrFE (7525) copolymer: 2. The effect of poling on curie transition and ferroelectric crystal structure, Polymer. 38 (1997) 4881–4889.
[20] H. Kim, F. Torres, Y. Wu, D. Villagran, Y. Lin, T.-L. Tseng, Integrated 3D printing and corona poling process of PVDF piezoelectric films for pressure sensor application, Smart Mater. Struct. 26 (2017), 085027, .
[21] S.K. Mahadeva, J. Berring, K. Walus, B. Stoeber, Effect of poling time and grid voltage on phase transition and piezoelectricity of poly(vinyledene fluoride) thin films using corona poling, J. Phys. D. Appl. Phys. 46 (2013) 285305.
[22] P.-H. Ducrot, I. Dufour, C. Ayela, Optimization of PVDF-TrFE processing conditions for the fabrication of organic MEMS resonators, Sci. Rep. 6 (2016) 19426.
[23] J. Li, C. Zhao, K. Xia, X. Liu, D. Li, J. Han, Enhanced piezoelectric output of the PVDF-TrFE/ZnO flexible piezoelectric nanogenerator by surface modification, Appl. Surf. Sci. 463 (2019) 626–634.
[24] J.S. Dodds, F.N. Meyers, K.J. Loh, Piezoelectric characterization of PVDF-TrFE thin films enhanced with ZnO nanoparticles, IEEE Sensors J. 12 (2012) 1889–1890.
[25] C. Chang, V.H. Tran, J. Wang, Y.-K. Fuh, L. Lin, Direct-write piezoelectric polymeric Nanogenerator with high energy conversion efficiency, Nano Lett. 10 (2010) 726–731.
[26] E. Ghafari, N. Lu, Self-polarized electrospun polyvinylidene fluoride (PVDF) nanofiber for sensing applications, Compos. Part B 160 (2019) 1–9.
[27] B. Ren, C.J. Lissenden, PVDF multielement lamb wave sensor for structural health monitoring, IEEE Trans. Ultrason. Ferroelectr. Freq. Control 63 (2016) 178–185.
[28] V.T. Rathod, G. Raju, L. Udpa, S. Udpa, Y. Deng, Multimode guided wave extraction capabilities using embedded thin film sensors in a composite laminated beam, Sens Actu. A 309 (2020) 112040.
[29] T. Siponkoski, M. Nelo, H. Jantunen, J. Juuti, A printable P(VDF-TrFE)-PZT composite with very high piezoelectric coefficient, Appl. Mater. Today 20 (2020) 100696.
[30] S. Guo, S. Chen, L. Zhang, W.H. Liew, K. Yao, Direct-write piezoelectric ultrasonic transducers for pipe structural health monitoring, NDT&E Int. 107 (2019) 102131.
[31] Z. Shen, S. Chen, L. Zhang, K. Yao, C.Y. Tan, Direct-write piezoelectric ultrasonic transducers for non-destructive testing of metal plates, IEEE Sensors J. 17 (2017) 3354–3361.
[32] G. Park, C.R. Farrar, Scalea FLD, S. Coccia, Performance assessment and validation of piezoelectric active-sensors in structural health monitoring, Smart Mater. Struct. 15 (2006) 1673–1683.
[33] S.J. Lee, H. Sohn, J.-W. Hong, Time reversal based piezoelectric transducer self-diagnosis under varying temperature, J. Nondestruct. Eval. 29 (2010) 75–91.
[34] Y. Kui, F.E.H. Tay, Measurement of longitudinal piezoelectric coefficient of thin films by a laser-scanning vibrometer, IEEE Trans. Ultrason. Ferroelectr. Freq. Control 50 (2003) 113–116.
[35] K. Kimura, H. Ohigashi, Generation of very high-frequency ultrasonic waves using thin films of vinylidene fluoride-trifluoroethylene copolymer, J. Appl. Phys. 61 (1987) 4749–4754.
[36] L.F. Brown, P(VDF-TrFE) films for high frequency ultrasonic transducers, Proceedings of SPIE - The International Society for Optical Engineering, 3664, 1999, pp. 31–34.
[37] S.W. Or, H.L.W. Chan, C.L. Choy, P(VDF-TrFE) copolymer acoustic emission sensors, Sens Actu. A 80 (2000) 237–241.
[38] P.W. Loveday, C.S. Long, D.A. Ramatlo, Ultrasonic guided wave monitoring of an operational rail track, Struct. Health Monit. 1475921719893887 (2019).
[39] F. Bargain, P. Panine, F. Domingues Dos Santos, S. Tencé-Girault, From solvent-cast to annealed and poled poly(VDF-co-TrFE) films: New insights on the defective ferroelectric phase, Polymer. 105 (2016) 144–156.
[40] R. Gregorio Jr., M.M. Botta, Effect of crystallization temperature on the phase transitions of P(VDF/TrFE) copolymers, J. Polym. Sci. B Polym. Phys. 36 (1998) 403–414.
[41] W. Li, L. Yu, Y. Zhu, D. Hua, J. Wang, L. Luo, et al., Annealing effect on poly(vinylidene fluoride/trifluoroethylene) (70/30) copolymer thin films above the melting point, J. Appl. Polym. Sci. 116 (2010) 663–667.
[42] M.H. Mohd Wahid, R. Mohd Dahan, S.Z. Sa'ad, A.N. Arshad, M.N. Sarip, M.R. Mahmood, et al., Effect of annealing temperature on the Crystallinity, morphology and ferroelectric of Polyvinylidenefluoride-Trifluoroethylene (PVDF-TrFE) thin film, Adv. Mater. Res. 812 (2013) 60–65.
[43] Y. Wu, X. Li, Y. Weng, Z. Hu, A.M. Jonas, Orientation of lamellar crystals and its correlation with switching behavior in ferroelectric P(VDF-TrFE) ultra-thin films, Polymer. 55 (2014) 970–977.
[44] J.S. Lee, A.A. Prabu, K.J. Kim, Annealing effect upon chain orientation, crystalline morphology, and polarizability of ultra-thin P(VDF-TrFE) film for nonvolatile polymer memory device, Polymer. 51 (2010) 6319–6333.
[45] Y.J. Park, S.J. Kang, C. Park, K.J. Kim, H.S. Lee, M.S. Lee, et al., Irreversible extinction of ferroelectric polarization in P(VDF-TrFE) thin films upon melting and recrystallization, Appl. Phys. Lett. 88 (2006) 242908.
[46] L. Qiu, M. Liu, X. Qing, S. Yuan, A quantitative multidamage monitoring method for large-scale complex composite, Struct. Health Monit. 12 (2013) 183–196.
[47] Y. Li, K. Wang, Q. Wang, J. Yang, P. Zhou, Y. Su, et al., Acousto-ultrasonics-based health monitoring for nano-engineered composites using a dispersive graphene-networked sensing system, Struct. Health Monit. (2020), https://doi.org/10.1177/1475921720929749.
[48] L. Fucai, M. Guang, K. Kageyama, S. Zhongqing, Y. Lin, Optimal mother wavelet selection for lamb wave analyses, J. Intell. Mater. Syst. Struct. 20 (2009) 1147–1161.
[49] J.P. Koduru, J.L. Rose, Transducer arrays for omnidirectional guided wave mode control in plate like structures, Smart Mater. Struct. 22 (2013) 015010.
[50] Z. Su, L. Ye, Identification of Damage Using Lamb Waves: From Fundamentals to Applications, Springer Science & Business Media, 2009.
[51] L. Qiu, S. Yuan, X. Zhang, Y. Wang, A time reversal focusing based impact imaging method and its evaluation on complex composite structures, Smart Mater. Struct. 20 (2011) 105014.
[52] S. Ha, F.-K. Chang, Adhesive interface layer effects in PZT-induced lamb wave propagation, Smart Mater. Struct. 19 (2010) 025006.